minerals

MDPI

Article

Two Epochs of Mineralization of Orogenic Gold Deposit in the East Kunlun Orogenic Belt: Constraints from Monazite U–Pb Age, In Situ Sulfide Trace Elements and Sulfur Isotopes in Wulonggou Gold Field

Zheming Zhang [1,2,3,4], Qingdong Zeng [1,3,4,*], Tong Pan [5], Hailin Xie [6], Zhanhao Wei [6], Hongrui Fan [1,3,4], Jinjian Wu [1,3,4], Kuifeng Yang [1,3,4], Xinghui Li [1,3] and Gaizhong Liang [1,3,4]

1 Key Laboratory of Mineral Resources, Institute of Geology and Geophysics, Chinese Academy of Sciences, Beijing 100029, China; zhangzheming17@mails.ucas.ac.cn (Z.Z.); fanhr@mail.iggcas.ac.cn (H.F.); wujinjian19@mails.ucas.ac.cn (J.W.); yangkuifeng@mail.iggcas.ac.cn (K.Y.); lxh@mail.iggcas.ac.cn (X.L.); lianggaizhong@mail.iggcas.ac.cn (G.L.)
2 Sinosteel Overseas Resources Limited, Sinosteel Group Corporation Limited, Beijing 100080, China
3 Innovation Academy for Earth Science, Chinese Academy of Sciences, Beijing 100029, China
4 College of Earth and Planetary Sciences, University of Chinese Academy of Sciences, Beijing 100049, China
5 Qinghai Geological and Mineral Exploration and Development Bureau, Xining 810008, China; pant66@163.com
6 The First Exploration Institute of Geology and Mineral Resources in Qinghai Province, Haidong 810600, China; dkjxhl@126.com (H.X.); qhszhw@163.com (Z.W.)
* Correspondence: zengqingdong@mail.iggcas.ac.cn

check for updates

Citation: Zhang, Z.; Zeng, Q.; Pan, T.; Xie, H.; Wei, Z.; Fan, H.; Wu, J.; Yang, K.; Li, X.; Liang, G. Two Epochs of Mineralization of Orogenic Gold Deposit in the East Kunlun Orogenic Belt: Constraints from Monazite U–Pb Age, In Situ Sulfide Trace Elements and Sulfur Isotopes in Wulonggou Gold Field. *Minerals* **2022**, *12*, 968. https://doi.org/10.3390/min12080968

Academic Editor: Stefano Salvi

Received: 28 June 2022
Accepted: 27 July 2022
Published: 29 July 2022

Publisher's Note: MDPI stays neutral with regard to jurisdictional claims in published maps and institutional affiliations.

Copyright: © 2022 by the authors. Licensee MDPI, Basel, Switzerland. This article is an open access article distributed under the terms and conditions of the Creative Commons Attribution (CC BY) license (https://creativecommons.org/licenses/by/4.0/).

Abstract: The Wulonggou Gold Field is one of the giant gold fields in the East Kunlun Orogenic Belt, northwestern China. Previous studies mainly focused on elementary mineral isotopic studies, fluid inclusions, and geological features in the Wulonggou Gold Field. In this study, we report some research on the precise age and the specific ore-forming process of the WGF: the hydrothermal monazite U–Pb ages; the way of gold precipitation; the composition, evolution, and source of ore-forming fluids of the Wulonggou Gold Field. Finally, we demonstrate a link between two-stage hydrothermal events and sequential episodes of crust-derived magmas, with implications for gold metallogeny in the East Kunlun Orogenic Belt. There are four hydrothermal stages that are recognized: a quartz–pyrite stage (stage 1), a quartz–pyrite–arsenopyrite–chalcopyrite stage (stage 2), a quartz–galena–sphalerite–pyrite stage (stage 3) and a quartz–stibnite–carbonate stage (stage 4). The monazite U–Pb ages of the Huanglonggou and Hongqigou deposits in the Wulonggou Gold Field were 422.2 ± 2.4 Ma and 236.7 ± 3.7 Ma, respectively, which support the opinion of two epochs of mineralization. Stages 1 and 2 are the main gold mineralization stages, wherein Au and As have a close genetic relationship. The Hongqigou and Huanglonggou deposits seem to have been formed in different metallogenic events due to the contrast on the trace element compositions in pyrite. The sources of the ore-forming materials and fluids of the Hongqigou and Huanglonggou deposits show apparent characteristics of orogenic gold deposit, and the magmatic events during Paleozoic and Mesozoic have an important contribution to the formation of the gold deposits. The gold deposits in the Wulonggou Gold Field can be interpreted as an orogenic gold system related to two-epoch tectonic–magmatic events.

Keywords: orogenic gold deposit; Wulonggou Gold Field; monazite U–Pb geochronology; pyrite trace element; in situ S isotope

1. Introduction

The Wulonggou Gold Field (WGF) is located ~65 km to the east of the Golmud City and is situated in the Middle Zone of the EKOB in tectonic setting (Figure 1B). Previous

studies mainly focused on elementary ore isotopic studies on bulk minerals, fluid inclusions in quartz, and geochronology research. In terms of the origin of ore-forming fluids and materials, metallogenic and pluton ages in the WGF (e.g., [1–3]), some authors suggested that the metallogenic events have a strong relationship with the Mesozoic magmatism [1–4], the majority of the authors suggested that the metallogenic events have a strong relationship with the Mesozoic magmatism [1–4], while fewer researchers have provided the evidence of Paleozoic metallogeny [2–4].

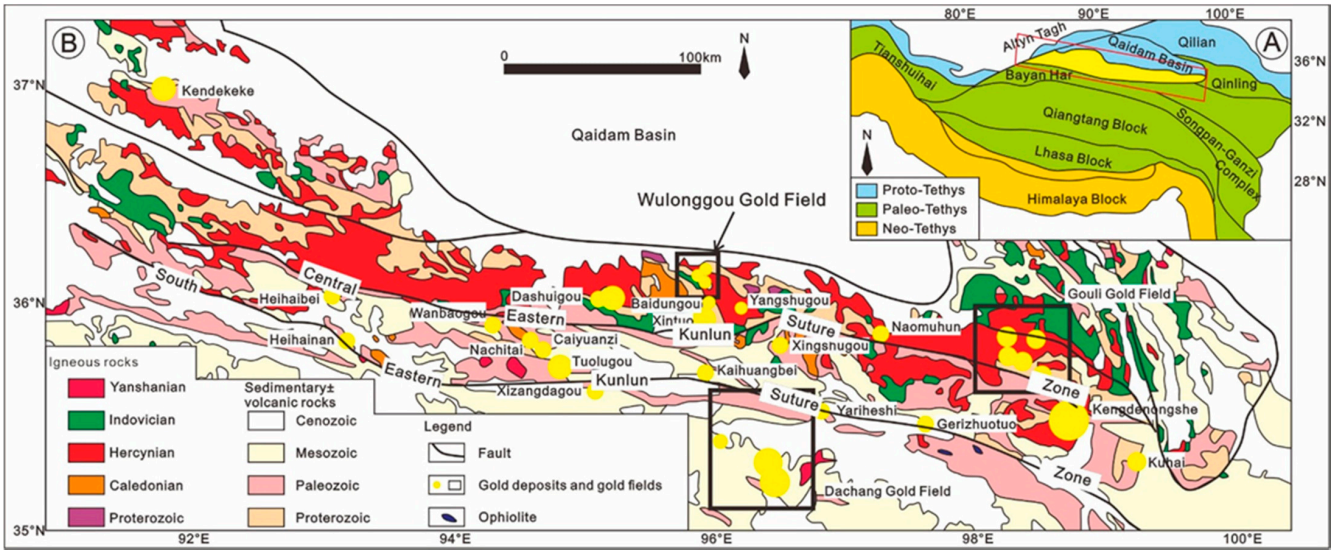


Figure 1. (**A**) The location of the East Kunlun Orogen Belt in the Qinghai–Tibetan plateau (modified after [5]). (**B**) Simplified Geological map of the East Kunlun Orogen Belt (modified after [5]).

However, some advanced research should be conducted to reveal the ore-forming process systematically and to know which tectonic setting these deposits are formed in by determining the metallogenic age by contemporaneous hydrothermal accessory minerals. In this paper, we report the results of the ore-forming age of the Wulonggou Gold Field, the evolution of the ore-forming fluids, and the sources of the fluids and metals. We studied sulfides from the Hongqigou and Huanglonggou gold deposits by using a combination of microscopy, laser ablation inductively coupled plasma mass spectrometry (LA-ICP-MS) for trace elements as well as mapping, multi-collector laser ablation inductively coupled plasma mass spectrometry (LA-MC-ICP-MS) for sulfur isotopic analysis, and backscattered electron (BSE) scanning microscopy. The LA-ICP-MS U–Pb analysis of monazite in Hongqigou and Huanglonggou deposits was carried out to determine the metallogenic ages. Moreover, we found the evidence of two epochs of mineralization and sequential episodes of crust-derived magmas in WGF through former analysis, which may provide some ideas of conducting research on gold metallogeny in the EKOB.

2. Geological Setting

The strata in the EKOB mainly include Proterozoic basement, Paleozoic sedimentary rocks interbedded with volcanic rocks, Mesozoic volcanic, and Cenozoic alluvial and pebbles (Figure 1B). The Proterozoic basement of the EKOB is composed of the Paleoproterozoic Jinshuikou, Kuhai, Wanbaogou, Baishahe groups and the Mesoproterozoic Xiaomiao Group [6–9]. The Jinshuikou Group (1.9~1.0 Ga) is characterized by granitic gneiss, migmatite, amphibolite and minor marble [8,10–12]. The Kuhai Group is composed of amphibolite, felsic gneiss, and marble [13]. The Wanbaogou Group is composed of clastic sediments, marble, and volcanic rocks, underwent greenschist face metamorphism [14]. The Baishahe Group is composed of amphibolite gneiss, mica-plagioclase gneiss, granulite, banded marble, mica schist, and mica-quartz schist [6]. The Mesoproterozoic Xiaomiao

Group is composed of quartzite, mica-quartz schist, biotite-plagioclase gneiss and marble [6]. The Paleozoic (Ordovician–Silurian) unit is related to the consumption of the Proto-Tethys and the subsequent collision between the northern and southern parts of the East Kunlun terranes [15], including the Maoniushan formation and Nachitai Group. The Ordovician–Silurian Maoniushan Formation consists of molasses, resting unconformably on pre-Ordovician–Devonian strata, which recorded the closure of the Proto-Tethys [16]. The Ordovician–Silurian Nachitai Group mainly consists of phyllite and other low-grade metavolcanic and meta-sedimentary rocks [17]. The Middle–Late Triassic Naocangjiangou and Xilikete Formations mainly consist of volcanic lava [18,19].

The East Kunlun Orogen is composed of the Northern East Kunlun Terrane and the Southern East Kunlun Terrane, which are separated by the Central East Kunlun Suture Zone. They are NWW–EW trending and north dipping and have the length of several hundred kilometers (Figure 1B). Two regional suture zones, the Central East Kunlun Suture Zone and Southern East Kunlun Suture Zone, which correspond to the evolution of the Proto-Tethys Ocean (Proterozoic–Early Paleozoic) and Paleo-Tethys Ocean (Late Paleozoic—Mesozoic), respectively, traverse the EKOB (e.g., [17]).

The mafic–ultramafic rocks mainly occur along the Central East Kunlun Suture Zone and Southern East Kunlun Suture Zone. The former was dated as Cambrian–Ordovician with ages that range from 537 Ma to 467 Ma (Figure 1B, [20–24]), whereas the latter was dated as both Cambrian–Ordovician (Figure 1B, 555–516 Ma, [25,26]) and Carboniferous ages (345–332 Ma, [26,27]). There are two epochs of granitoids range from 460–430 Ma and 290–190 Ma in the EKOB: the former recorded the Early Paleozoic terrane accretion history between Gondwana and Laurasia that was driven by the northward subduction of the Proto-Tethys oceanic crust until final closure ([28–34] and references therein); the latter records a complete evolution history from the sea-floor spreading of the Paleo-Tethys Ocean to northward subduction, then collided, and finally was the post-collisional magmatism ([29,31,33–36] and references therein).

3. Ore Deposit Geology

The WGF is structurally controlled by three synclinoria and three NW-trending sinistral ductile shear zones (Figure 2). The strata of the WGF include the Paleoproterozoic Jinshuikou Group, Mesoproterozoic Xiaomiao and Neoproterozoic Qiujidonggou formations, Early Ordovician ultramafic rocks, Late Silurian–Early Devonian granitoids and dolerite dykes, Late Permian–Late Triassic gabbro, diorite, granitoids, and metavolcanic rocks (Figure 2). The Jinshuikou Group (1927 ± 34 Ma, [6]) mainly consists of plagioclase gneiss, with minor migmatite, schist, marble, amphibolite, and granulite [2,9]. The Xiaomiao Formation (1683–1554 Ma, [37]) consists of marble, gneiss, amphibolite, granulite, schist, quartzite [2,9]. The Neoproterozoic Qiujidonggou Formation is composed of meta-conglomerate, metasandstone, schist, phyllite and marble [2,9,38]. The Ordovician Qimantage Group ultramafic rocks (zircon U–Pb age of 486.5 ± 3.4 Ma, [38]) are mainly composed of clinopyroxenites and porphyritic hornblendites intruded by porphyritic hornblende gabbro dykes and granite dykes. The Quaternary mainly distribute in ravines and valleys.

The intrusive rocks in the WGF formed during the Neoproterozoic, Early Paleozoic, Late Paleozoic and Early Mesozoic (Figure 2). The majority of intrusive rocks in the WGF formed during Early Paleozoic, which mainly include brick-red coarse-grained syenogranite with minor diorite. Their ages range from 450 to 410 Ma, and some A-type granites are about 390 Ma [1,2,39,40]. The Early Mesozoic intrusive rocks are epigenetic granite. Late Silurian-Early Devonian granitoid batholiths are composed of dominantly granodiorites and syenogranites, and the granodiorites contain abundant mafic micro-granular enclaves (MMEs) (Figure 2, [39]). Late Permian–Late Triassic intrusions intruded into Precambrian metamorphic rocks or Paleozoic magmatic rocks, and comprise gabbro-diorite complexes, diorite-granodiorite batholiths, and porphyritic granodiorite stocks and porphyritic quartz diorite dykes (Figure 2). The porphyry and diorite porphyrite veins show LA-ICP-MS

zircon U–Pb age of about 220 Ma [39]. Metavolcanic rocks include tuff and minor amounts of volcanic breccia and are considered to have formed in the Late Triassic according to a zircon U–Pb age of 219 ± 1 Ma [39].

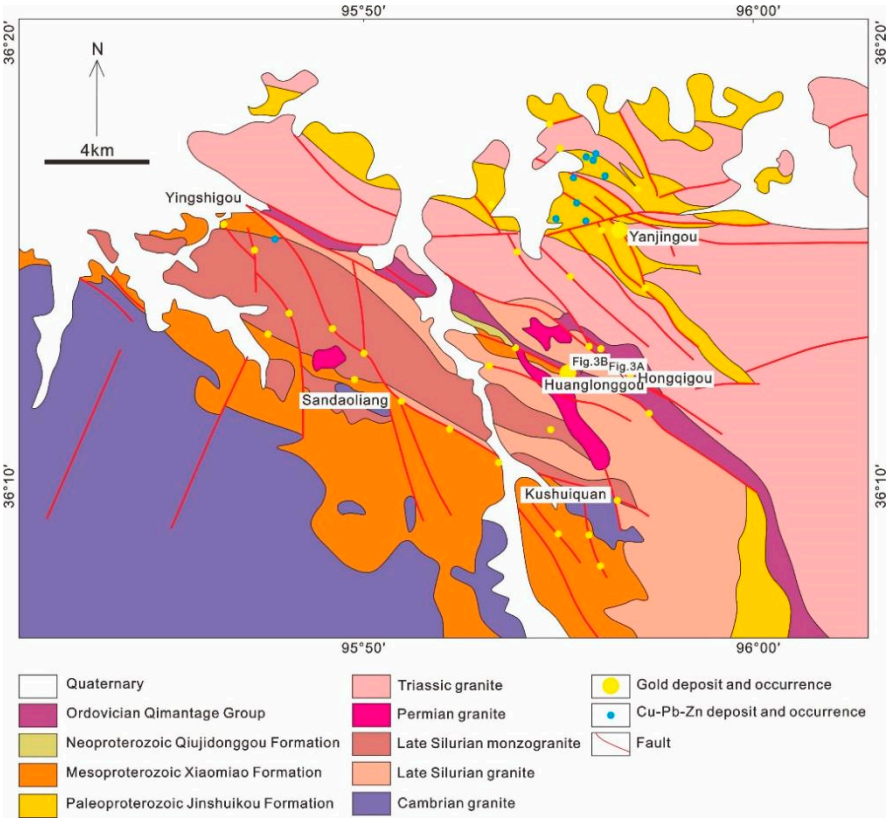


Figure 2. Geological map of the Wulonggou Gold Field (modified after [9]).

There are three ore belts of Yanjingou, Yingshigou–Hongqigou and Sandaoliang–Kushuiquan, from north to south, respectively. They are controlled by the brittle structural fracture zones hosted in the pre-existed NW-trending ductile shear zones, and they were formed during Triassic. They are 0.5–2 km in width, 10–20 km in length, and have a dip angle of ~70° NE. The majority of gold deposits in the area are distributed within or close to these three ductile shear zones (Figure 2). The Yanjinggou ore belt has ore bodies of lengths of over 5 km, widths of 0.5~1 km, and a dip to 35°~75° NE [4]. The Yingshigou–Hongqigou ore belt, located in the middle of the ore field, is the best gold mineralized ore belt in the Wulonggou area. The orebodies have lengths of over 5 km, widths of 1~2 km, and a dip to 55°~85° NE [4]. There are above 65 t gold in this belt, the gold reserve of Hongqigou is 15 t, with an average gold grade of 6.9 g/t; the gold reserve of the Huanglonggou deposit is 29.3 t, with an average gold grade of 9.39 g/t (from the work report completed by the First Exploration Institute of Geology and Mineral Resources in Qinghai Province). The Hongqigou and Huanglonggou deposits we discussed in this paper are located in this belt. The dip angle of orebodies in the Hongqigou deposit is relatively slower than that of the Huanglonggou deposit (Figure 3). Sandaoliang–Kushuiquan ore belt, located in the southmost part of the WGF, the orebodies have lengths of more than 10 km and widths of 0.5~1 km, and a dip to 45°~70° NE [4]. The Hongqigou and Huanglonggou gold deposits are located in the largest Yingshigou–Hongqigou gold belt in central WGF. Gold mineralization in these gold deposits is characterized by multi-stage quartz–sulfide veins containing abundant invisible gold.

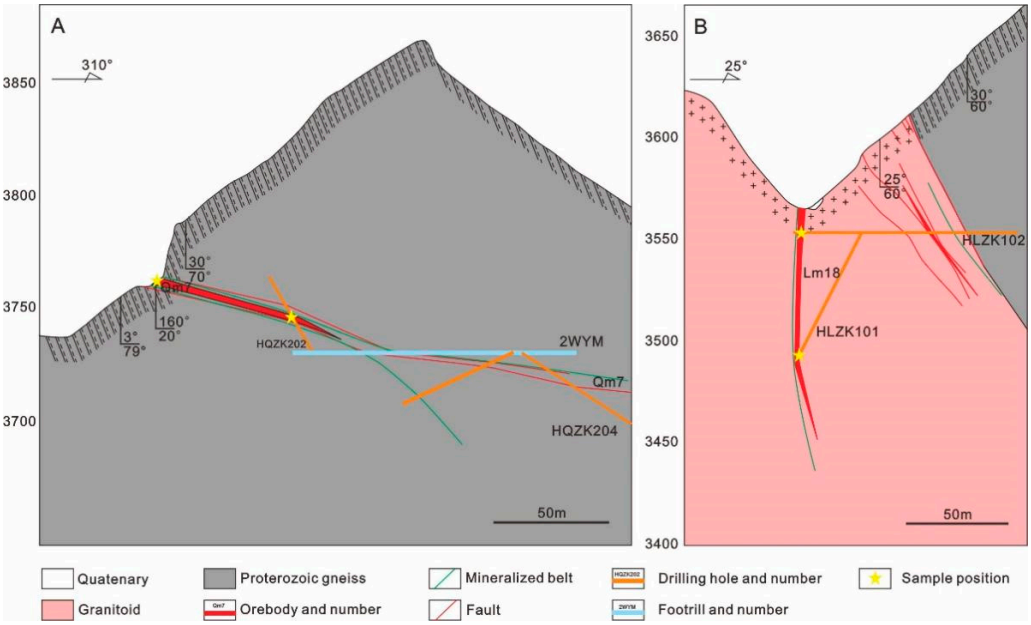


Figure 3. Profiles of the 2nd prospecting line of the Hongqigou deposit (**A**) and the 1st prospecting line of the Huanglonggou deposit (**B**) (modified after the map drawn by Qinghai Geological and Mineral Exploration and Development Bureau, 2015).

A total of 80 samples of each stage ores were collected from the tunnels of 3330 m, 3390 m, 3450 m above sea level and drilling cores in the Huanglonggou deposit, and orebodies' outcrops of 3600 m to 3800 m above sea level and drilling cores in the Hongqigou deposit.

The gold mineralization of other gold deposits in the WGF is confined in the altered and fractured zones, within which the metallic minerals are predominantly native gold, pyrite, pyrrhotite, arsenopyrite, sphalerite, galena, chalcopyrite, lollingite, and marcasite; gangue minerals are mainly quartz, sericite, chlorite, calcite, and fluorite; hydrothermal alteration includes mainly silicification, chloritization, sericitization, and carbonatization [1–4]. The gold deposits in this ore field yield age of ~240 Ma (sericite Ar-Ar, [41]; quartz Rb-Sr, [4]).

Paragenetic Sequences

Paragenetic sequences and crosscutting relationships indicate different ore-forming events in the Hongqigou and Huanglonggou deposits (Figures 4 and 5). The ore-forming process can be divided into four hydrothermal stages (Figures 4 and 5): a quartz–pyrite stage (stage 1), a quartz–pyrite–arsenopyrite–chalcopyrite stage (stage 2), a quartz–galena–sphalerite–pyrite stage (stage 3) and a quartz–stibnite–carbonate stage (stage 4). Gold mainly occurs in invisible gold in pyrite and arsenopyrite, such as cation exchange or tiny grains that are difficult to observe under a microscope and SEM; this will draw a conclusion in Section 5.3.1 through trace element mapping of pyrite. By comparing the paragenetic association of minerals, we can find that minor sphalerite but major galena is in the ores of stage 3 of the Hongqigou deposit, and that minor galena but major sphalerite is in the ores of stage 3 of the Huanglonggou deposit; the Huanglonggou deposit has more chalcopyrite in ores, while the Hongqigou deposit has more arsenopyrite in ores (Figures 4–6). Silicification and sericitization were closely related to gold mineralization.

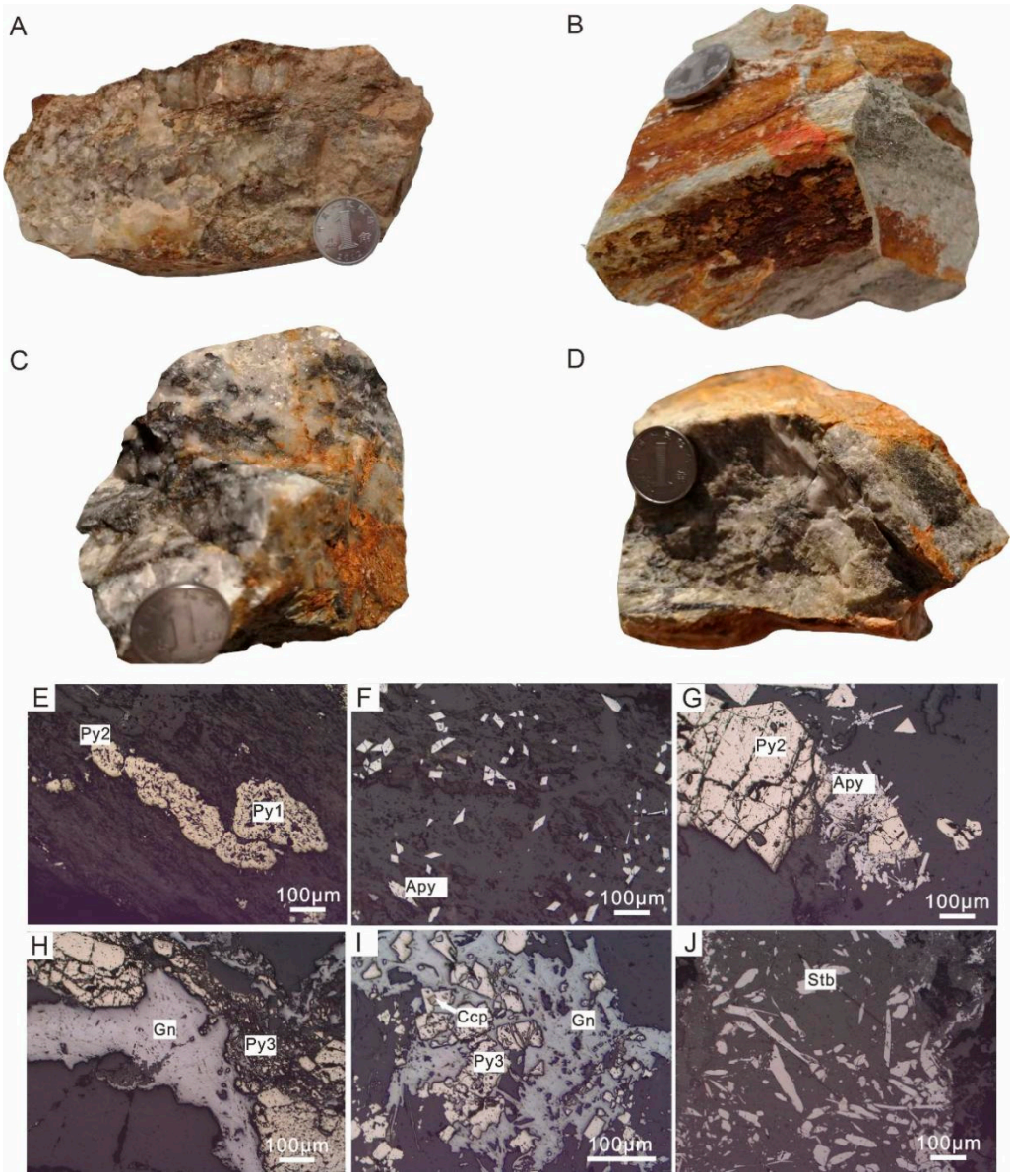


Figure 4. Photos of the ore of each stage and micrographs showing paragenesis associations in the Hongqigou deposit. (**A**) Typical barren quartz of stage 1; (**B**) Typical quartz–pyrite–arsenopyrite–chalcopyrite ore of stage 2; (**C**) Typical quartz–galena–pyrite ± arsenopyrite ore of stage 3, which represent the major lead, zinc, and silver metallogenic period; (**D**) Typical quartz–stibnite–carbonate ore of stage 4; (**E**) Rough and porous Py1 was contained by smooth Py2; (**F**) Arsenopyrite spread in stage 2 ores; (**G**) Euhedral–subhedral Py2 was crosscut by arsenopyrite in stage 2; (**H**) Subhedral Py3 was altered by galena; (**I**) Subhedral Py3 was interfilled by galena and chalcopyrite; (**J**) Stibnite spread in quartz-stibnite-carbonate ores in stage 4. Abbreviations: Apy = arsenopyrite, Ccp = chalcopyrite, Gn = galena, Py = pyrite, Stb = stibnite.

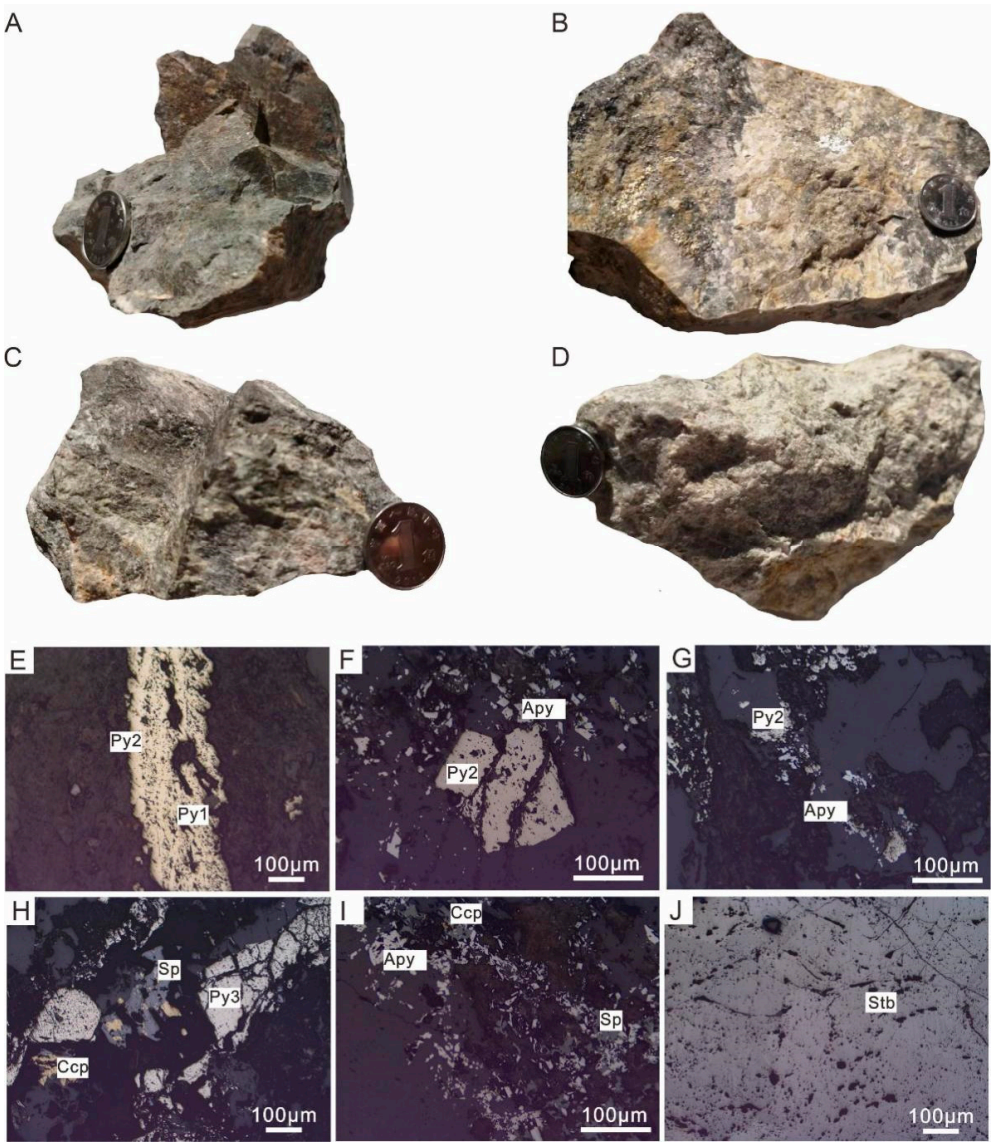


Figure 5. Photos of the ore of each stage and micrographs showing paragenesis associations in the Huanglonggou deposit. (**A**) Typical crushed altered rock type ore of stage 1; (**B**) Typical quartz-pyrite–arsenopyrite–chalcopyrite ore of stage 2; (**C**) Typical quartz–sphalerite–pyrite ± arsenopyrite ore of stage 3, which represent the major lead, zinc and silver metallogenic phase; (**D**) Typical quartz–stibnite–carbonate ore of stage 4; (**E**) Rough and porous Py1 was contained by smooth Py2; (**F**) Euhedral–subhedral Py2 was crosscut by arsenopyrite in stage 2; (**G**) Arsenopyrite and pyrite coexist in ores of stage 3; (**H**) Subhedral Py3 was interfilled by sphalerite and chalcopyrite; (**I**) Subhedral sphalerite and chalcopyrite coexist with euhedral arsenopyrite in stage 3; (**J**) Stibnite spread in quartz–stibnite–carbonate ores in stage 4. Abbreviations: Apy = arsenopyrite, Ccp = chalcopyrite, Py = pyrite, Sp = sphalerite, Stb = stibnite.

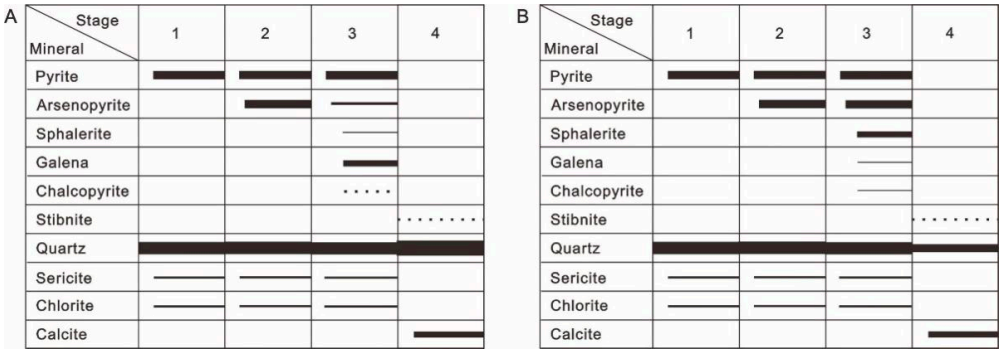


Figure 6. Paragenetic sequences for major minerals of the Hongqigou deposit (**A**) and the Huanglonggou deposit (**B**).

4. Analytical Method

4.1. Mineralogy

Doubly polished thin-sections (0.2 mm thick) were made from auriferous quartz veins for petrographic study of compositions, textures, structures, and spatial distributions of minerals. Detailed mineral identification was carried out by scanning electron microscopy (SEM) using the TM4000 plus SEM system at the Institute of Geology and Geophysics, Chinese Academy of Sciences (IGGCAS), which is equipped with a Bruker Quantax 75 energy spectrum to identify and confirm different minerals and observe special textures. Backscattered electron images (BSE) were acquired at 20 kV, and a high vacuum environment illustrated the alteration and the texture between the ore minerals and the gangue minerals. The acquisition time for each BSE image was 1 min, and the monazite used for U–Pb metallogenic age dating was observed and screened in this way. Moreover, we divided the mineralization stage, and distinguished the different types of pyrite by using the above method.

4.2. Monazite U–Pb Dating

Hydrothermal monazite, which was closely related to Au mineralization, was found by using SEM and was applied to in situ LA-ICP-MS U–Pb dating. Monazite U–Pb dating was conducted using an Agilent 7500a Q-ICP-MS equipped with a Geolas G2 193 nm excimer laser ablation system (Geolas HD, Lambda Physik, Göttingen, Germany) at IGGCAS. The analyses were conducted with a spot size of 24 μm and at a repetition rate of 8 Hz. Each analysis incorporated approximately 20 s of background acquisition and 45 s of data acquisition. The standard samples Namaqualand and Jefferson were applied to correct the U/Pb fractionation and the instrumental mass discrimination for the external standard and were measured after every six samples. All measured $^{206}Pb/^{238}U$, $^{208}Pb/^{232}Th$, $^{207}Pb/^{235}U$ and $^{207}Pb/^{206}Pb$ isotopic ratios of the Namaqualand during sample analyses were corrected and regressed afterwards [42]. We calibrated the isotopic and elemental fractionation and instrument quality deviations using Glitter 4.0 software for the calibration [43].

4.3. In Situ Sulfide Trace Element Analysis and Mapping

In situ pyrite trace element analysis and mapping were conducted using LA-ICP-MS at the State Key Laboratory of Ore Deposit Geochemistry, Institute of Geochemistry, Chinese Academy of Sciences (IGCAS), China. Laser sampling was performed by ASI RESOLution-LR-S155 laser microprobe equipped with a Coherent Compex-Pro 193 nm ArF excimer laser. We used Agilent 7700 × ICP-MS to acquire ion signal intensities. The carrier gas was He (350 mL/min). Before exiting the cell, the ablated aerosol was mixed with Ar (900 mL/min) as the transport gas. Each analysis includes approximately 30 s of background acquisition (gas blank), followed by 60 s of sample data acquisition. The analysis was performed at a pit diameter of 26 μm, a pulse frequency of 5 Hz, and a flux of 3 J/cm^2. STDGL3 was used to determine the concentration of siderophile and chalcophile elements [44]. The in-house

standard pure pyrite (Py) was used to calibrate the concentrations of Fe and S; GSE-1G and GSD-1G were used for calibrating and converting the comprehensive count data of the concentrations of lithophile elements. We took the sulfide reference substance MASS-1 as an unknown sample for verifying the accuracy of the analysis. Trace elements that are relative to gold metallogeny such as ^{59}Co, ^{60}Ni, ^{65}Cu, ^{66}Zn, ^{75}As, ^{107}Ag, ^{121}Sb, ^{197}Au, ^{208}Pb, ^{209}Bi, ^{125}Te were determined and mapped.

4.4. In Situ Sulfide Sulfur Isotope Analysis

In situ pyrite sulfur isotopic analyses were performed at the Wuhan Sample Solution Analytical Technology Co., Ltd., Wuhan, China. We used a Neptune Plus MC-ICP-MS equipped with a Geolas HD excimer ArF laser ablation system. Helium was used as the carrier gas of the ablation unit in the laser ablation system, which was mixed with Ar (supplement gas) after the ablation unit. A single point ablation mode was used. A large spot size (44 μm) and slow pulse frequency (2 Hz) were applied to avoid downhole step effects, as reported by [45]. There were 90 laser pulses applied on each sample. A new signal smoothing device was applied downstream of the sample pool, which eliminated the short-term variation of the signal effectively, especially in the case of the slower pulse frequency [46]. The laser flux was stable at 5 J/cm^2. Neptune Plus came with nine Faraday cups and with a $10^{11}\Omega$ resistor. Isotopes ^{32}S and ^{34}S were collected in the Faraday cup using static mode. Newly designed X Skimmer cones and JET sample cones were used on Neptune Plus to improve signal strength. In all, 4 mL/min nitrogen was added to the central flow to reduce polyatomic interference. All measurements were made using rotational power (defined as peak-edge widths of 5%–95% of the full peak height) at a median resolution consistently >5000. The pyrite standard PPP-1 bracketing method (SSB) was applied for correcting instrumental mass fractionation. The $\delta^{34}S_{V\text{-}CDT}$ reference values of the standards have been reported by [45], and the analysis of S isotopic ratios was conducted by using the software of "Iso-Compass" [47].

5. Results

5.1. In Situ U–Pb Geochronology of Monazite

The in situ U–Pb dating analyses on monazite grains of the Huanglonggou and Hongqigou were presented in Table 1 and Figures 7 and 8. The U–Pb data were shown on the Tera–Wasserburg concordia diagram. The lower intercept age of Hongqigou was 236.7 ± 3.7 Ma (MSWD = 0.33) (Figure 7), and the lower intercept age of Huanglonggou was 422.2 ± 2.4 Ma (MSWD = 0.16) (Figure 8). Most of the analyzed monazite grains were together with pyrite grains of stage 2 (Figures 7 and 8). On the other hand, quartz and sericite are often wrapped in monazite minerals, which shows that the monazite is not the residue of the wall rocks, but the hydrothermal mineral crystalized together with quartz–pyrite–chalcopyrite vein (Figures 7 and 8). Therefore, their crystallization ages can represent the timing of gold mineralization, which is consistent with the age of granite porphyry and suggests their close genetic relationship.

Table 1. The results of the LA–ICP–MS U–Pb dating on hydrothermal monazite in the Wulonggou gold field.

Hongqigou Deposit								
Spot Number	**^{207}Pb/^{206}Pb**	**Error**	**^{206}Pb/^{238}U**	**Error**	**^{207}Pb/^{235}U**	**Error**	**^{208}Pb/^{232}Th**	**Error**
Hongqigou-1	0.42256	0.00545	0.08213	0.00126	4.79008	0.04848	0.0183	0.00025
Hongqigou-2	0.5193	0.00466	0.11783	0.00164	8.44495	0.06124	0.01918	0.00026
Hongqigou-3	0.47555	0.0068	0.09846	0.0016	6.46213	0.07121	0.01847	0.00026
Hongqigou-4	0.47919	0.00611	0.10034	0.00155	6.63648	0.0658	0.01921	0.00027
Hongqigou-5	0.49759	0.00637	0.10905	0.0017	7.48896	0.07435	0.01864	0.00026
Hongqigou-6	0.34584	0.00356	0.06569	0.00093	3.13573	0.02615	0.01761	0.00024

Table 1. *Cont.*

Hongqigou Deposit								
Spot Number	$^{207}Pb/^{206}Pb$	**Error**	$^{206}Pb/^{238}U$	**Error**	$^{207}Pb/^{235}U$	**Error**	$^{208}Pb/^{232}Th$	**Error**
Hongqigou-7	0.4282	0.0058	0.08395	0.00132	4.96137	0.05246	0.01814	0.00025
Hongqigou-8	0.46357	0.00766	0.09491	0.00164	6.07223	0.07702	0.01658	0.00024
Hongqigou-9	0.29419	0.0048	0.05799	0.00095	2.35443	0.03106	0.01898	0.00027
Hongqigou-10	0.45555	0.00944	0.0924	0.00181	5.80953	0.09164	0.01667	0.00024
Hongqigou-11	0.43754	0.00607	0.08783	0.00139	5.30415	0.05731	0.01682	0.00023
Hongqigou-12	0.56724	0.00588	0.15324	0.00223	11.99711	0.09862	0.02323	0.00032
Hongqigou-13	0.59236	0.00727	0.18292	0.00286	14.95476	0.14364	0.02494	0.00035
Huanglonggou deposit								
Spot Number	$^{207}Pb/^{206}Pb$	**Error**	$^{206}Pb/^{238}U$	**Error**	$^{207}Pb/^{235}U$	**Error**	$^{208}Pb/^{232}Th$	**Error**
Huanglonggou-1	0.07582	0.00082	0.07033	0.00091	0.73646	0.00692	0.02172	0.00029
Huanglonggou-2	0.11618	0.00135	0.07539	0.001	1.20969	0.01209	0.02214	0.0003
Huanglonggou-3	0.05336	0.00105	0.06733	0.00094	0.49625	0.00913	0.02198	0.0003
Huanglonggou-4	0.12753	0.00155	0.07672	0.00103	1.35138	0.01411	0.02182	0.00029
Huanglonggou-5	0.08696	0.001	0.07166	0.00094	0.86071	0.00867	0.02251	0.0003
Huanglonggou-6	0.07261	0.00514	0.0695	0.00197	0.69693	0.04652	0.01675	0.00023
Huanglonggou-7	0.14143	0.00165	0.07886	0.00106	1.54043	0.01526	0.02374	0.00032
Huanglonggou-8	0.07181	0.0009	0.06962	0.00092	0.6905	0.00773	0.02183	0.00029
Huanglonggou-9	0.07122	0.00074	0.06938	0.0009	0.6825	0.00608	0.02181	0.00029
Huanglonggou-10	0.06378	0.00067	0.06877	0.00089	0.60583	0.00554	0.02049	0.00027
Huanglonggou-11	0.05834	0.00075	0.06798	0.00089	0.54775	0.00634	0.02032	0.00027
Huanglonggou-12	0.07682	0.00161	0.06981	0.00103	0.74073	0.01423	0.02069	0.00029
Huanglonggou-13	0.10698	0.00144	0.07428	0.00101	1.09761	0.01294	0.01785	0.00024

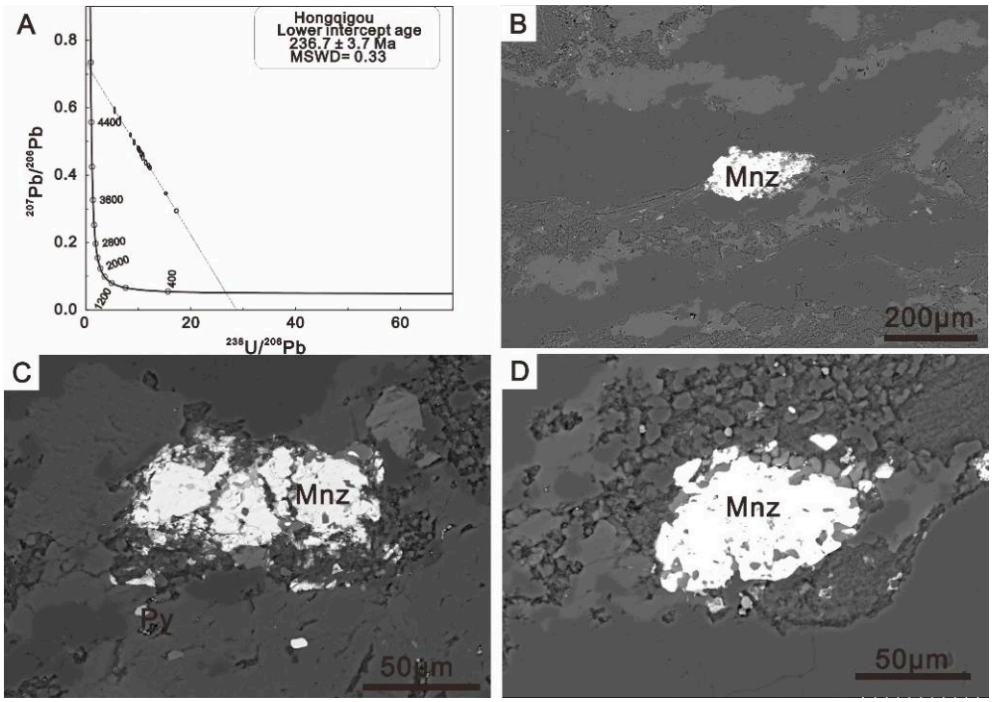


Figure 7. (**A**) The U–Pb Tera–Wasserburg Concordia diagram of monazite in the Hongqigou deposit; (**B**–**D**) BSE images of typical monazite grains in stage 2 ores of the Hongqigou deposit. Abbreviations: Mnz = monazite.

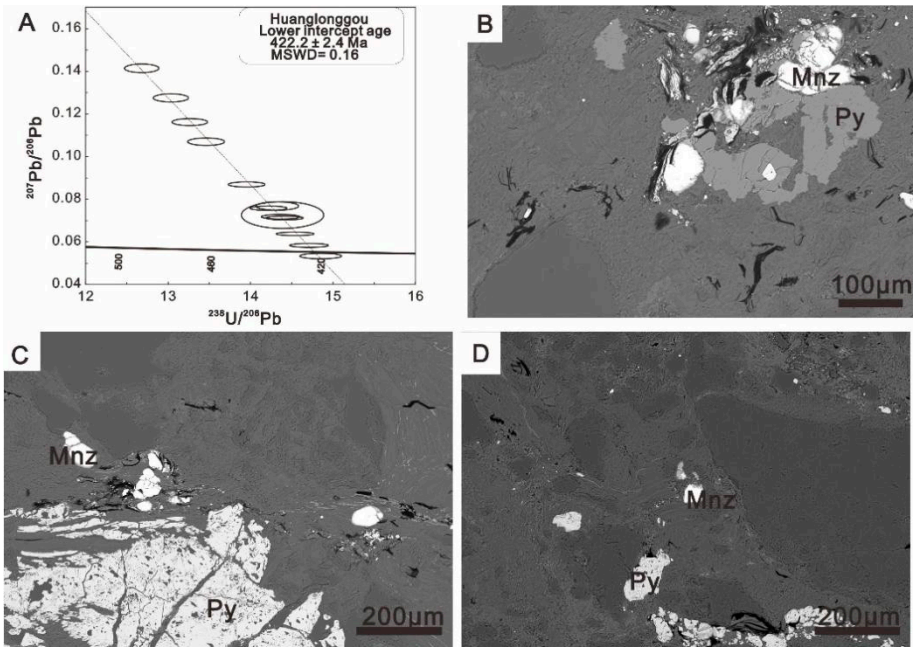


Figure 8. (**A**) The U–Pb Tera–Wasserburg Concordia diagram of monazite in the Huanglonggou deposit; (**B**–**D**) BSE images of typical monazite grains coexist with pyrite in stage 2 ores of the Huanglonggou deposit. Abbreviations: Mnz = monazite, Py = pyrite.

5.2. Generation and Texture of Pyrite

Based on optical characteristics and BSE observation, these kinds of pyrite and pyrrhotite were recognized: Py0 (pyrite in ultra-mylonite), Po (pyrrhotite in schist), Py1, Py2, Py3 (pyrite in ores of different stages from early to late) (Figure 9).

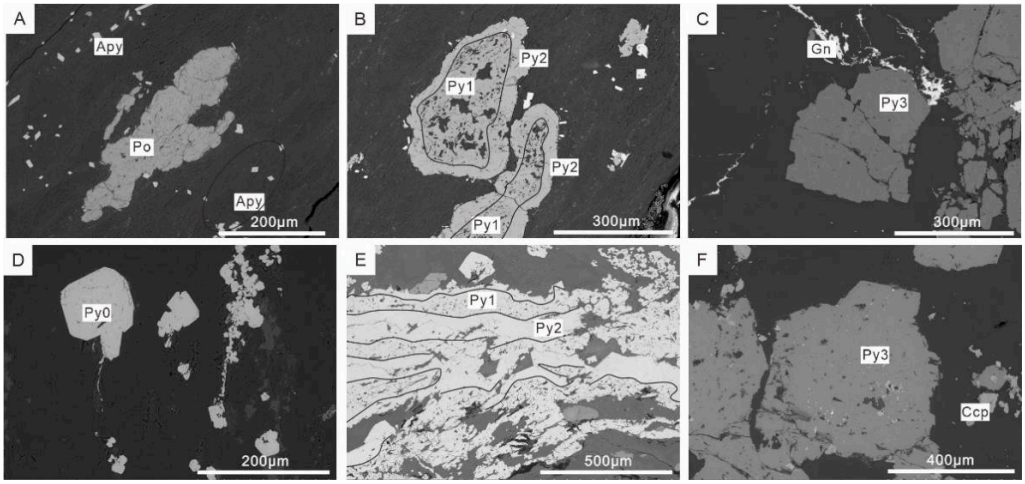


Figure 9. BSE images of sulfides of each stage. (**A**) Pyrrhotite in the schist of wall rock; (**B**) Rough and porous Py1 was contained by smooth Py2 in the Hongqigou deposit; (**C**) Py3 coexist with galena in stage 3 in the Hongqigou deposit; (**D**) Py0 in ultra-mylonite; (**E**) Rough and porous Py1 was contained by smooth Py2 in the Huanglonggou deposit; (**F**) Py3 coexist with chalcopyrite in stage 3 in the Huanglonggou deposit. Abbreviations: Apy = arsenopyrite, Ccp = chalcopyrite, Gn = galena, Po = pyrrhotite, Py = pyrite.

Py0 (pyrite in ultra-mylonite) and Po (pyrrhotite in schist) occurs as subhedral–anhedral crystals, which distribute parallelly.

Pyrite 1 (Py1) occurs as elongated anhedral crystals, which distribute parallelly, this may be a result of the deformation process. Numerous randomly oriented silicate inclusions

dominated by sericite and quartz can be observed within Py1. This kind of pyrite commonly occurs in alteration zones, often being the core with Py2 and Py3 surrounding it as a rim. This suggests that Py1 is the earliest pyrite accompanying the pyrite–sericite–quartz alteration (stage 1).

Pyrite 2 (Py2), with little silicate inclusions, commonly overgrows Py1, and the pyrite may also be deformed. It occurs as coarse subhedral–anhedral grains and often has a smooth surface. Some Py1 grains without Py2 rims are accompanied with fine quartz crystals and surrounded by later coarse quartz veins, indicating Py2 precipitated during stage 2.

Pyrite 3 (Py3) occurs either as anhedral or subhedral clusters without zoning. It shows paragenetic relationships with chalcopyrite, galena, and sphalerite. These characteristics suggest that Py3 formed during stage 3.

5.3. Trace Element Distribution in Sulfide

5.3.1. Mapping of the Py1 and Py2 in the Hongqigou and Huanglonggou Deposits

The relationship between the two generations of pyrite is shown in Figure 9 where Py1 is earlier than Py2, as clearly distinguished in both optical and BSE images.

In the Hongqigou deposit, Py2 (rim) has richer As, Au, Cu and Bi and lower Co, Ni, Pb, Sb than that of Py1 (core) (Figure 10). The distribution of Pb in Py1 and the distribution of Co and Ni seem not uniform, which suggests the existence of mineral inclusions (Figure 10). We can find that the Au content in arsenopyrite is relatively higher than that of pyrite (Figure 10), suggesting that Au in the Hongqigou deposit may be carried by Au–As complexes.

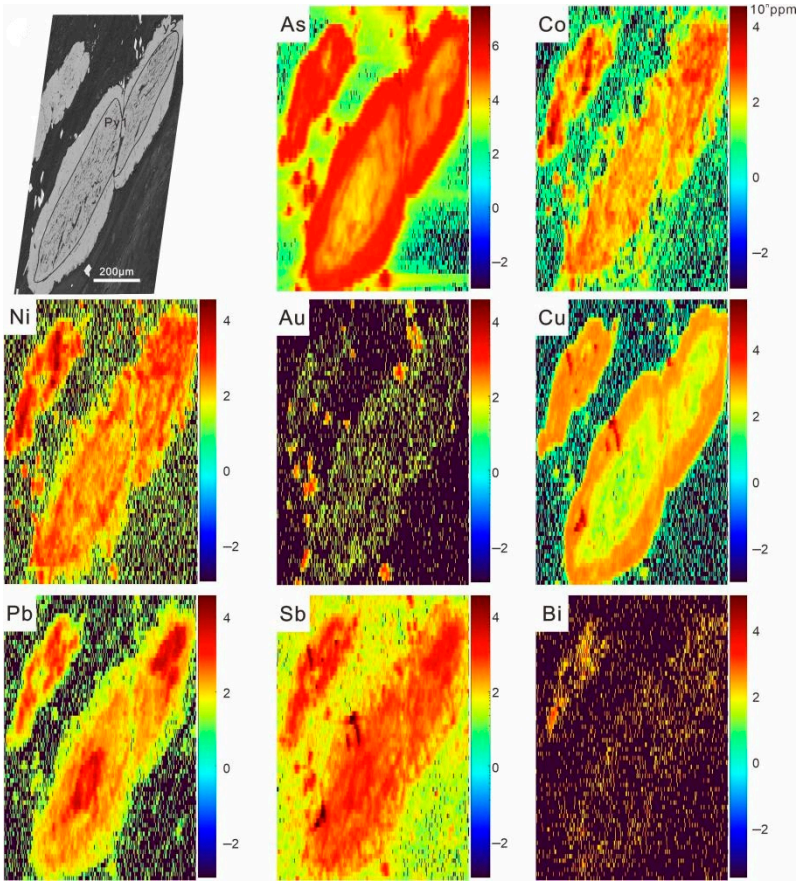


Figure 10. The LA-ICP-MS elemental mapping of Py in the Hongqigou deposit, BSE image of the selected pyrite, other pictures: element distribution of each element.

In the Huanglonggou deposit, Py2 (smooth face) has richer Sb and lower As, Co, Ni, Cu, Pb, Bi than that of Py1 (rough face) (Figure 11), and the distribution of Au is similar in these two kinds of pyrite. Some inclusions that are rich in Cu, Pb may exist in Py1 because of their nonuniform distribution (Figure 11).

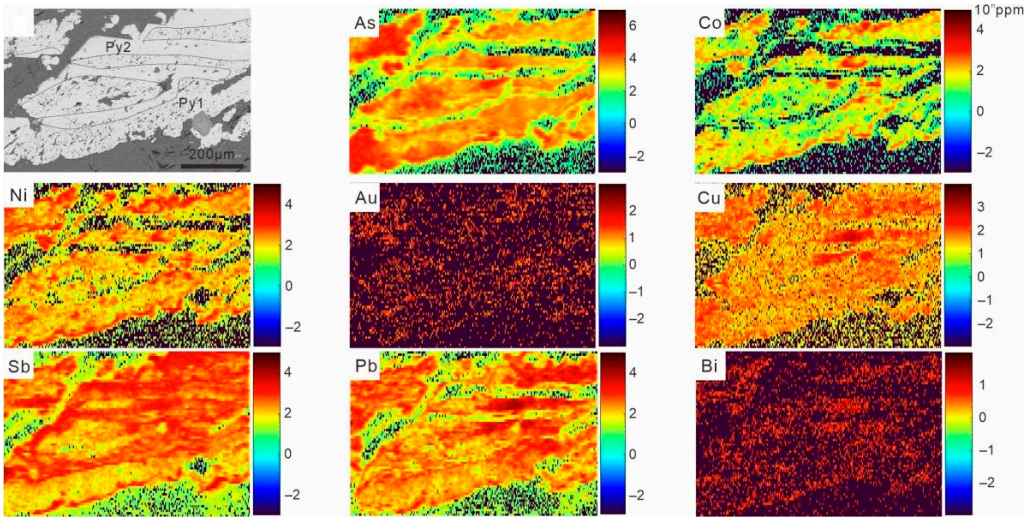


Figure 11. The LA-ICP-MS elemental mapping of Py in the Huanglonggou deposit, BSE image of the selected pyrite, other pictures: element distribution of each element.

5.3.2. In Situ Trace Element Analysis

Pyrite is one kind of important gold-bearing mineral. Hence, the Au content in different types of pyrite is crucial. We determined the trace elements in pyrites of each stage. We also determined the trace elements of sulfides in wall rock (pyrrhotite in schist and pyrite in ultra-mylonite) for contrast.

A total of 68 analyzed spots were obtained on pyrite and pyrrhotite among different stages. It is important and necessary to avoid the influence and faults carried by mineral inclusions (e.g., native gold, silicate or sulfide inclusions) when designing analysis spots, while some inclusions below the surface are difficult and unavoidable to detect, which brought some outliers. Absolute concentrations (ppm) of selected trace elements in pyrite are reported in Table 2 and Appendix A Table A1; the significant changes of trace elements are illustrated in Figures 12 and 13.

Table 2. The summarized LA-ICP-MS analytical results of trace elements for different generations of pyrite in each stage and pyrrhotite in schist of wall rock in the WGF (ppm, bdl = below detection limit).

		^{59}Co	^{60}Ni	^{65}Cu	^{66}Zn	^{75}As	^{107}Ag	^{121}Sb	^{125}Te	^{197}Au	^{208}Pb	^{209}Bi
Pyrrhotite in schist (n = 8)	Min	326.323	591.205	bdl.	bdl.	bdl.	bdl.	0.178	bdl.	bdl.	0.155	0.367
	Max	491.131	1073.904	1.949	7.117	4.594	2.240	15.199	0.461	0.124	8.720	13.182
	Median	431.729	812.913	0.773	2.840	1.818	1.093	4.338	0.077	0.052	3.069	4.630
Pyrite in ultra-mylonite (n = 8)	Min	73.199	30.788	25.344	0.937	455.063	2.355	bdl.	114.985	bdl.	bdl.	23.681
	Max	2090.737	1663.032	2124.885	8.683	6884.256	18.771	3.657	196.658	2.841	0.512	110.829
	Median	925.406	566.395	554.571	5.002	2371.613	6.766	1.829	155.343	0.494	0.138	47.744
Py1 in Hongqigou (n = 6)	Min	23.159	25.736	119.957	bdl.	21,440.451	bdl.	80.295	bdl.	0.790	17.017	0.084
	Max	55.921	103.544	360.547	3.328	56,807.293	2.491	480.888	2.123	1.691	148.769	0.256
	Median	34.156	50.335	234.019	1.568	35,862.411	1.004	234.779	0.623	1.337	65.914	0.154
Py2 in Hongqigou (n = 10)	Min	57.332	102.625	185.494	bdl.	40,115.177	bdl.	51.747	bdl.	0.263	10.809	0.068
	Max	159.267	242.640	607.798	146.296	76,993.084	5.901	491.204	1.869	3.447	121.852	0.621
	Median	90.756	157.615	423.802	16.280	54,278.866	1.303	189.854	0.338	1.023	46.533	0.358

Table 2. *Cont.*

		^{59}Co	^{60}Ni	^{65}Cu	^{66}Zn	^{75}As	^{107}Ag	^{121}Sb	^{125}Te	^{197}Au	^{208}Pb	^{209}Bi
Py3 in Hongqigou (n = 9)	Min	0.036	bdl.	0.737	bdl.	2262.859	bdl.	1.632	bdl.	bdl.	3.974	0.638
	Max	46.389	21.510	15.724	3.974	5223.606	9.880	265.700	8.308	0.751	857.226	35.190
	Median	10.758	7.550	3.483	0.981	3363.130	2.742	54.684	2.031	0.221	139.826	6.971
Py1 in Huanglonggou (n = 10)	Min	14.371	16.091	10.330	bdl.	671.534	bdl.	bdl.	99.793	bdl.	bdl.	60.713
	Max	203.787	313.391	86.059	15.131	8871.994	47.119	29.734	916.985	2.416	1.414	1210.961
	Median	88.777	136.476	46.229	5.476	4503.607	20.885	5.286	366.128	0.501	0.592	568.107
Py2 in Huanglonggou (n = 8)	Min	0.707	4.625	1.232	bdl.	250.834	bdl.	bdl.	10.803	bdl.	bdl.	4.263
	Max	135.063	147.200	54.534	79.576	13,275.196	19.131	11.649	460.266	1.229	0.592	269.836
	Median	26.475	58.107	20.032	11.410	4338.190	6.487	3.080	152.824	0.310	0.369	95.117
Py3 in Huanglonggou (n = 9)	Min	7.310	2.107	2.135	bdl.	612.995	bdl.	bdl.	3.573	bdl.	0.128	15.335
	Max	27.731	69.971	14.968	5.692	11,409.009	13.659	11.823	42.921	2.615	4.304	1853.086
	Median	11.855	19.506	7.214	1.188	5566.746	9.096	3.438	16.193	0.599	1.714	452.719

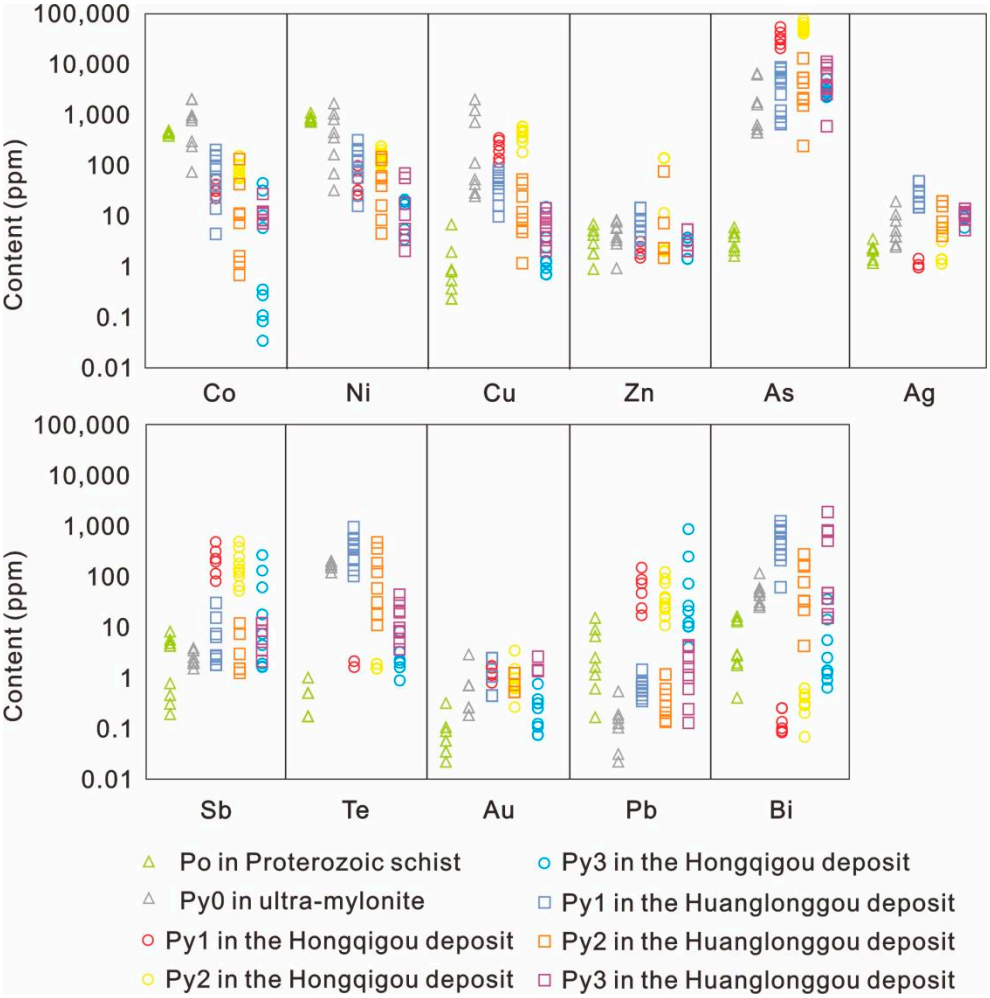


Figure 12. The variation ranges of trace elemental contents in pyrite and arsenopyrite determined by LA-ICP-MS.

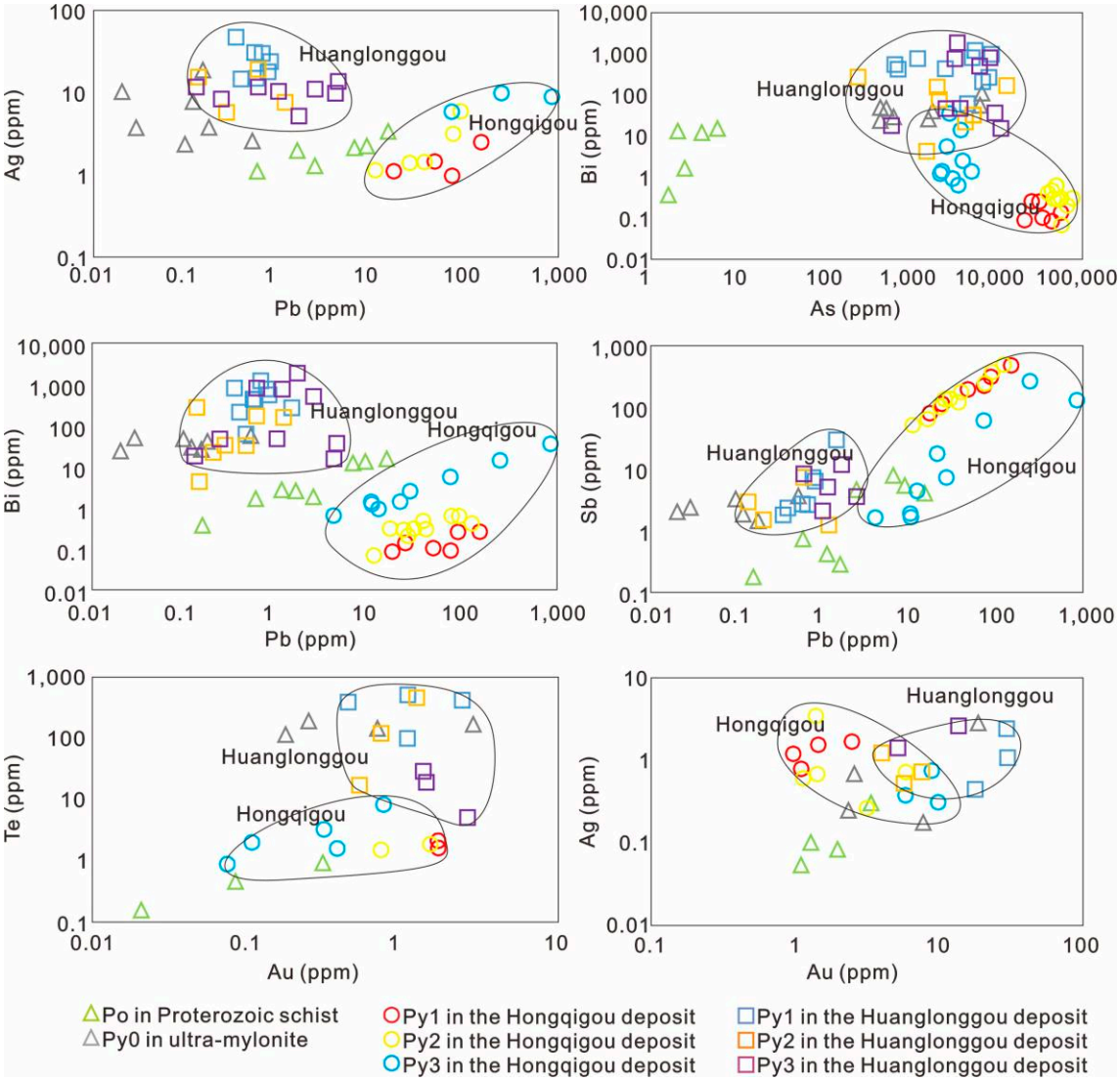


Figure 13. The selected binary plots showing the geochemical characteristics of pyrite from each stage of ores in the Hongqigou and Huanglonggou deposits, ultra-mylonite, and pyrrhotite in schist of wall rock.

5.4. Sulfur Isotopic Data on Sulfide

Sulfur isotopic data of seven types of pyrite are compiled in Table 3 and shown in Figure 14. The pyrrhotite in schist and pyrite in ultra-mylonite have $\delta^{34}S$ values and range from +6.92‰ to +9.90‰ and 2.39‰ to 3.48‰, respectively. The $\delta^{34}S$ values of Py1 Py2 and Py3 of the Hongqigou deposit range from +1.00‰ to +1.19‰, +0.95‰ to +1.22‰ and +10.91‰ to +11.66‰, respectively. The $\delta^{34}S$ values of Py1, Py2 and Py3 of the Huanglonggou deposit range from −2.94‰ to −0.68‰, +4.00‰ to +4.74‰ and +2.75‰ to +3.63‰, respectively.

Table 3. The summarized LA-ICP-MS analytical results of sulfur isotope ratios for different generations of pyrite in each stage and pyrrhotite in schist of wall rock in the WGF (ppm, bdl = below detection limit).

Sample Name	δ^{34}Sv-CDT (‰)	Delta-2SE	Sample Name	δ^{34}Sv-CDT (‰)	Delta-2SE
Schist-Po-1	9.30	0.08	Hongqigou-Py3-3	11.52	0.10
Schist-Po-2	8.95	0.11	Hongqigou-Py3-4	11.66	0.09
Schist-Po-3	7.16	0.09	Hongqigou-Py3-5	11.61	0.10
Schist-Po-4	7.00	0.08	Hongqigou-Py3-6	10.91	0.09
Schist-Po-5	6.92	0.10	Hongqigou-Py3-7	11.48	0.09
Schist-Po-6	9.90	0.09	Hongqigou-Py3-8	11.54	0.10
Schist-Po-7	7.68	0.10	Hongqigou-Py3-9	11.28	0.11
Schist-Po-8	9.67	0.08	Huanglonggou-Py1-1	−1.63	0.10
Ultramylonite-Py-1	2.70	0.22	Huanglonggou-Py1-2	−2.94	0.11
Ultramylonite-Py-2	2.92	0.19	Huanglonggou-Py1-3	−1.65	0.09
Ultramylonite-Py-3	2.39	0.27	Huanglonggou-Py1-4	−1.78	0.11
Ultramylonite-Py-4	3.30	0.20	Huanglonggou-Py1-5	−1.95	0.11
Ultramylonite-Py-5	3.48	0.19	Huanglonggou-Py1-6	−2.61	0.10
Ultramylonite-Py-6	2.78	0.20	Huanglonggou-Py1-7	−1.72	0.09
Ultramylonite-Py-7	2.68	0.17	Huanglonggou-Py1-8	−2.35	0.12
Ultramylonite-Py-8	2.87	0.16	Huanglonggou-Py1-9	−2.34	0.10
Hongqigou-Py1-1	1.07	0.10	Huanglonggou-Py1-10	−0.68	0.21
Hongqigou-Py1-2	1.09	0.09	Huanglonggou-Py2-1	4.00	0.09
Hongqigou-Py1-3	1.13	0.09	Huanglonggou-Py2-2	4.74	0.09
Hongqigou-Py1-4	1.19	0.10	Huanglonggou-Py2-3	4.67	0.07
Hongqigou-Py1-5	1.00	0.08	Huanglonggou-Py2-4	4.55	0.08
Hongqigou-Py1-6	1.01	0.09	Huanglonggou-Py2-5	4.15	0.08
Hongqigou-Py2-1	1.16	0.09	Huanglonggou-Py2-6	4.70	0.08
Hongqigou-Py2-2	1.17	0.08	Huanglonggou-Py2-7	4.17	0.08
Hongqigou-Py2-3	1.02	0.07	Huanglonggou-Py2-8	4.26	0.08
Hongqigou-Py2-4	0.95	0.08	Huanglonggou-Py3-1	3.12	0.08
Hongqigou-Py2-5	1.08	0.09	Huanglonggou-Py3-2	3.14	0.10
Hongqigou-Py2-6	1.22	0.09	Huanglonggou-Py3-3	3.06	0.11
Hongqigou-Py2-7	1.15	0.10	Huanglonggou-Py3-4	2.75	0.10
Hongqigou-Py2-8	1.20	0.08	Huanglonggou-Py3-5	3.63	0.11
Hongqigou-Py2-9	0.98	0.09	Huanglonggou-Py3-6	2.97	0.10
Hongqigou-Py2-10	1.15	0.08	Huanglonggou-Py3-7	2.81	0.12
Hongqigou-Py3-1	11.62	0.09	Huanglonggou-Py3-8	3.21	0.11
Hongqigou-Py3-2	11.43	0.10	Huanglonggou-Py3-9	2.89	0.09

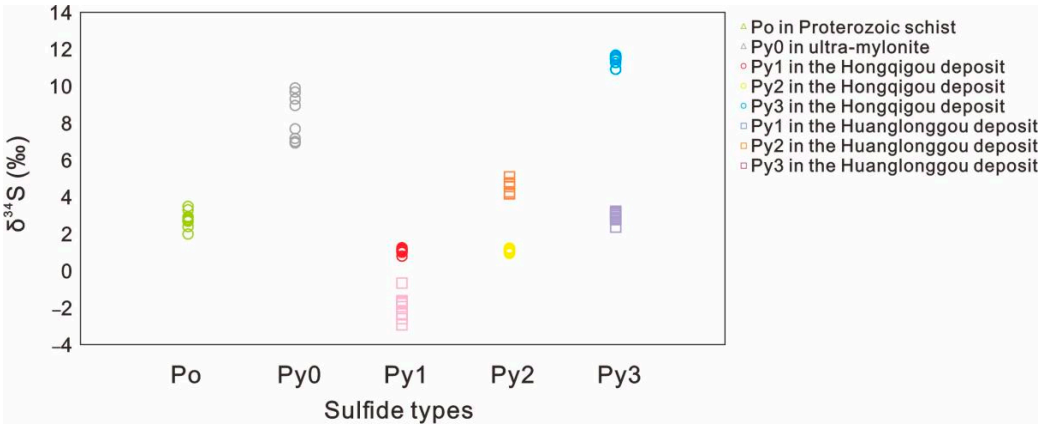


Figure 14. The δ^{34}S values of pyrite from each stage of ores in the Hongqigou and Huanglonggou deposits, ultra-mylonite, and pyrrhotite in schist of wall rock.

6. Discussion

6.1. Evolution of Pyrite Textures and Compositions

6.1.1. Mineral Paragenesis and Evolution

The classification of the different mineralization stages in this study is based on a detailed analysis of mineral assemblage, structure, and intersecting relationship. The main metallogenic stages 1 and 2 were represented by fractured altered rock type mineralization, during which there was a strong tectonic deformation, resulting in the fragmentation of the orebody and the orientation of minerals. Polymetallic sulfides were rich in stage 3, including chalcopyrite, sphalerite, and galena (Figure 9). At stage 4, stibnite, quartz, and calcite appeared. Pyrite occurs in all mineralization stages; arsenopyrite is often apparent in stages 1 and 2, which are rich in gold, while the amount of gold and arsenopyrite is negligible in stages 3 and 4. From stages 1 to 4, the complete metallogenic evolution process from early-to-late stages can be traced: the content of pyrite decreased, and their crystal morphology changed from oriented anhedral grains to euhedral—subhedral grains (Figure 9). Thus, our observations and results suggest that the metallogenic environment changed from a relatively stable environment in the early stage to a compression background, and then to a repeatedly turbulent and open environment, and finally returned to stability.

6.1.2. Relationship and Evolution of Trace Elements in Hongqigou and Huanglonggou Deposits

According to a vast literature, analysis of the trace elements (i.e., As, Au, Ag, Bi, Co, Cu, Pb, Zn, Ni, Sb, and Te) in pyrite can be used to distinguish the occurrence states of each element [48–51], know about the composition changes of ore-forming fluids [52–55], and analyse the physical and chemical changes of ore-forming fluids and growth history [50,56–59].

Some scholars suggest that gold partitioning into pyrite depends on As availability, as the Au–As coupled substitution is a key for Au precipitation (e.g., [60–64]). However, the arsenian pyrite (high As concentration) does not always record high Au values because it is obvious that the As-rich fluids are not invariably Au-bearing (e.g., [63,65]). These phenomena can be found in this paper: Au contents in pyrite from the Hongqigou and Huanglonggou deposits were similar, while the As content in Hongqigou deposit was much higher than that of Huanglonggou. Co and Ni enter the lattice via isomorphic substitution of Fe, whereas As, Te, Sb, and Bi enter the lattice substituting for S. The concentrations of Te, Sb, and Bi are extremely low and possibly caused by the high As concentration. We can find that the Te, Sb, and Bi contents of Huanglonggou were much higher than that of Hongqigou, whereas the As content represents a contrasting tendency. Hence, the compositions of the ore-forming fluids of the Hongqigou and Huanglonggou deposits seem to be different, and this may suggest that they formed in two different metallogenic events. The Au and As are rich in Py2 of the Hongqigou deposit, while in the Huanglonggou deposit, the contents of Au and As in Py1 were higher than that of Py2, which may suggest that the main Au metallogenic event in the Hongqigou happened in magmatic-hydrothermal process, while the wall-rock alteration may be the key to the mineralization in the Huanglonggou deposit. We would draw these conclusions after discussing metals ratios and sulfur isotopes. This might be further solid evidence of multiple mineralization beside ore-forming age.

Except for high Co and Ni values, other elements in Po were low (Figures 12 and 13). The contents of Co, Ni, Cu, Te, and Bi in Py0 are high, while that of Zn, As, Sb, and Pb are relatively low. In the Huanglonggou deposit, the contents of Co, Ni, Cu, Zn, Ag, and Te in Py1, Py2, and Py3 decrease successively, indicating that metal in ore-forming fluids gradually unloaded from early stage to late stage. In Hongqigou deposit, Co, Ni, Cu, and As elements increased slightly from Py1 to Py3 and then decreased sharply, while the contents of Sb and Bi gradually increased, indicating that strong precipitation occurred at stage 2. By comparing the trace elements in different stages of the Hongqigou and Huanglonggou deposits, it can be found that Cu, As, Sb, and Pb elements in the Hongqigou deposit are higher than those in the Huanglonggou deposit, especially in Stage 1 and Stage

2 (Figures 12 and 13). The Ag, Te, and Bi elements in the Hongqigou deposit are lower than those in the Huanglonggou deposit, indicating that the composition and evolution trend of the ore-forming fluids of the two deposits can be distinguished easily (Figures 12 and 13).

6.1.3. Source of Ore-Forming Materials

The ratio between different elements was generally applied upon determining the source of pyrite, and even deducing the evolution of the metallogenic stage and the genesis of the deposit. The Co/Ni ratio of pyrite has a great signature on ensuring the change of metallogenic environment, especially on the source of hydrothermal gold deposits [52,66,67]. The contents of Co and Ni in pyrite can be relatively high in the deposits that are related to mafic intrusions and contributed by degassing [68,69]. The high Co/Ni ratio of magmatic source is generally higher than that of pyrite formed in sedimentary environment [52,68,69]: magmatic–hydrothermal pyrite exhibits high Co/Ni ratios of > 1, whereas sedimentary–diagenetic pyrite has low Co/Ni ratios of < 1 [69]. The correlation between Au and As in pyrite can be applied for knowing the types of gold deposits: generally, the Au/As ratio of pyrite in orogenic gold deposits is relatively low (< 0.004, [53]), that of Carlin-type and magmatic gold deposits seems to be high [48]. The $\delta^{34}S$ values of pyrite are usually used as tracers of the sources of ore-forming materials and discussing the ore-forming processes [70,71]. Different sulfur reservoirs have their typical $\delta^{34}S$ value ranges: (1) magmatic source of sulfur (magma: −3‰ to +7‰, [72,73]; andesite, 1.0 ± 6.1‰, [74]; granitoids: 2.6 ± 2.3‰, [75]) (2) sedimentary rocks reduced sulfur (<0, [76]) and (3) marine (20‰, [76]). Generally, the source of ore-forming materials and fluids of orogenic gold deposits was commonly considered to be of a metamorphic origin with some materials from intrusive rocks [77–79]. The majority $\delta^{34}S$ values of orogenic gold deposits around the world have a range from 0 to +10‰ [80]. Hence it is difficult to determine the source of ore-forming materials and the evolution of ore deposits simply by using sulfur isotopic composition. Accordingly, we need to determine the source of ore-forming materials and processes by combining some of the trace elements and S isotopic composition of pyrite and pyrrhotite in ores of each metallogenic stages and wall rocks.

The Co/Ni ratios of Po were lower than 1 (0.457~0.613), suggesting the schist were mainly formed in sedimentary and metamorphic process; the Co/Ni ratios of Py0 have a wide range of 0.233~9.706 and have both magmatic and sedimentary characters, which represent that the ultra-mylonite formed during ductile-brittle shearing, when some magma was transported upwards. The available Au/As ratios in Po have a range of 0~0.027, suggesting a mixed origin of magma and metamorphism; and the Au/As ratios Py0 have a range of 0~1.7 × 10^{-3}, all of them lower than 0.004, suggesting obvious characteristics of orogenic gold deposit. The $\delta^{34}S$ values of Po and Py0 in schist and ultra-mylonite shows narrow ranges (+1.99‰ to +3.48‰ and 6.92‰ to 9.90‰, respectively). These characteristics suggest that Po originated from deep magmatic fluids and metamorphic fluids, and that Py1 mainly came from metamorphic fluids.

Hongqigou

The Co/Ni ratios of Py1 and Py2 are generally lower than 1 (0.540~1.003, 0.399~0.714, respectively), which are similar to that of Po, suggesting a similar source: sedimentary/metamorphic environment; the Co/Ni ratios of Py3 have a wide range of 0.066~2.359, suggesting a mixed source. The Au/As ratios in Py1, Py2, and Py3 have ranges of 1.8 × 10^{-5}~6.5 × 10^{-5}, 0.5 × 10^{-5}~5.1 × 10^{-5}, and 0~2.6 × 10^{-4}, respectively, all of which are lower than 0.004, suggesting obvious characteristics of orogenic gold deposit.

The $\delta^{34}S$ values of Py1 (+1.00‰ to +1.19‰) and Py2 (+0.95‰ to +1.22‰) in Hongqigou vary in a narrow range, suggesting a magmatic source. The $\delta^{34}S$ values of Py3 (+10.91‰ to +11.66‰) in Hongqigou seems to be higher than those of Py1 and Py2, indicating a participation of wall rock materials, because the $\delta^{34}S$ values of Py3 are quite similar to those of Po in schist.

Huanglonggou

The Co/Ni ratios of Py1, Py2, and Py3 have wide ranges of 0.223~3.352, 0.041~2.380, and 0.1771~5.826, respectively, which suggest a mixed source of sedimentary/metamorphic and magmatic origin. The Au/As ratios in Py1, Py2, and Py3 have ranges of 0~3.6 $\times$ 10^{-4}, 0~5.6 $\times$ 10^{-4}, and 0~4.1 $\times$ 10^{-4}, respectively, all of them lower than 0.004, suggesting obvious characteristics of orogenic gold deposit.

The $\delta^{34}S$ values of Py1 (−2.94‰ to −0.68‰), Py2 (+4.00‰ to +4.74‰), and Py3 (+2.75‰ to +3.63‰) in Huanglonggou vary in a narrow range, but there are certain differences between them, suggesting the magmatic–metallogenic process may be characterized by a multi-stage pulse, into which some wall rock materials have been mixed.

6.2. Tectonic Evolution and Mineralization

Researchers [81] promoted a long-lived subduction and accretionary tectonic model to interpret tectonic evolution of the EKOB. There were a subduction and accretionary complex and a back-arc basin during the Early Paleozoic—Triassic period. The Central Kunlun Belt was split from the Qaidam Block to an Early Paleozoic island-arc due to the spreading of the Qimantagh back-arc basin in response to the northward subduction of the Kunlun Ocean. During the Early Paleozoic—Triassic period, the EKOB evolved into a trench-arc-back-arc basin tectonic system and composite orogenic processes, which include a wide accretionary complex and long-lived northward subduction.

During ca. 460–430 Ma (Figure 15A), coevally with the ongoing northward subduction of the Kunlun oceanic slab, the oceanic crust of the Qimantage back-arc basin began to subduct towards the north beneath the Qaidam terrane [81], These processes indicate that the arc-type and subduction-related magmatic events were widespread and intense during the Ordovician–Silurian period in the EKOB. Due to northward subduction of the Kunlun oceanic slab, the island-arc of EKOB has been thickened and developed numerous gabbroic–granitic intrusions and its products [81,82].

When the Qimantage back-arc basin closed, the Central Kunlun island-arc and the Qaidam Block collided at ca. 425 Ma (Figure 15B), and the ocean crust detached from the continental crust, these processes generated syn-collisional plutons in the northern Central Kunlun Belt and the North Qimantage Belt [81]. The Huanglonggou gold deposit in this study (422.2 $\pm$ 2.4 Ma) and the Tuolugou Co–Au polymetallic deposit in the EKOB formed in this period of tectonic setting.

At ca. 400 Ma (Figure 15C), the EKOB began to delaminate from the overthickened lithosphere and a series of post-collisional plutonic magmas intruded [81,83].

During the Carboniferous–Permian period (Figure 15D), because of the delamination and post-orogenic collapse, the regional extent of the belt had transitioned from compression to extension, as well as the northward subductions of the Kunlun oceanic slab [81]. The gold deposits of Annage, Guoluolongwa in the EKOB formed during this period.

During ca. 270–250 Ma (Figure 15E), the northward subduction of the Kunlun oceanic plate had been reactivated, which resulted in the intrusions of gabbro, diorite and voluminous I-type granite in the Central Kunlun Belt [81].

During ca. 250–220 Ma (Figure 15F), slab break-off of the ongoing northward subduction of the Kunlun oceanic plate had taken place, which is evidenced by massive granitoids with MMEs in the Central Kunlun Belt; the slab break-off led to the upwelling of the mantle-derived magma from the asthenosphere, which was underplated beneath the crust of the Central Kunlun arc; this can be supported by the abundant granitic intrusions [81]. This period is the most important and largest scale metallogenic event in the EKOB. The Hongqigou gold deposit in this study (236.7 $\pm$ 3.7 Ma) and other major gold/polymetallic deposits, such as Heishigou, Kengdenongshe, Xingshugou, Baidungou, Yanjingou, Dashuigou, Asiha, Naomuhun, Kendekeke, Xizangdagou, Dachang, were all formed in this period. We prepose that its metallogenic event is related to the subduction of the EKOB, an opinion which is also supported in some previous studies [84].

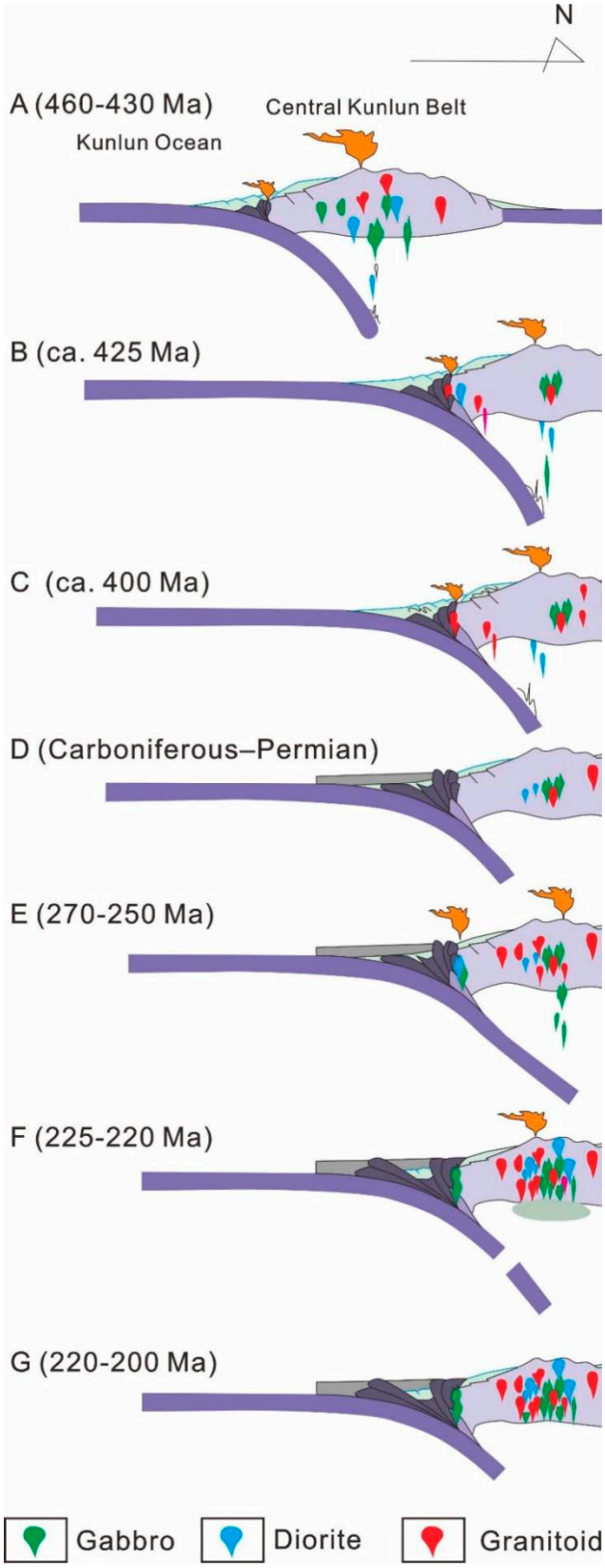


Figure 15. Schematic diagram showing the metal deposits formed in the geodynamic setting in the EKOB (modified after [81]).

During ca. 220–200 Ma (Figure 15G), the Central Kunlun arc underwent a collapse in response to underplating, and A-type granites generated at that same time, which suggests a post-collision setting [81]. Manite gold deposit in the EKOB formed during this period.

Therefore, there are two metallogenic epochs in WGF: Silurian–Devonian deposits were mainly hosted in the ductile-brittle shear zones, while the Middle–Late Triassic deposits were mainly hosted in the NW-trending brittle fractures.

6.3. Magmatism and Mineralization

In terms of the formation time, orogenic gold deposits show several prominent peaks in the late Archean to Paleoproterozoic and Phanerozoic orogenic belts [77,85]. The EKOB records two epochs of orogenesis, corresponding to the evolution of the Neoproterozoic to late Paleozoic Proto-Tethys Ocean and late Paleozoic to Triassic Paleo-Tethys Ocean [27]. In this paper, we determined the monazite U–Pb age of the Huanglonggou deposit (422.2 ± 2.4 Ma) and the Hongqigou deposit (236.7 ± 3.7 Ma), indicating that there were two epochs of magmatic—metallogenic events happening in the WGF.

The age data of the gold deposits in the EKOB have been collected (Table 4), which build up an objective geochronological framework for gold mineralization in the EKOB. There are two epochs of gold mineralization that have been recognized in the EKOB: Silurian–Devonian and Middle–Late Triassic events, and they are distinct geographically in ore fields and belts. Only a few of deposits in the EKOB reported to be formed during Silurian–Devonian period, such as the Annage, Guoluolongwa gold deposits and Tuolugou Co–Au deposit (429–374 Ma). The Middle–Late Triassic deposits are mainly located in the EKOB, such as Baidungou, Heishigou, Kengdenongshe, Xingshugou, Hongqigou, Yanjingou Dashuigou, Asiha, Naomuhun, Kendekeke, Xizangdagou, Dachang, Manite gold deposits (244–213 Ma). The granitoids in the Wulonggou gold district mostly display zircon U–Pb ages of ca. 438–390 Ma and 260–211 Ma [31,86–99]. Consequently, the main gold metallogenic event of the EKOB is Middle–Late Triassic.

Table 4. Ages of the EKOB gold deposits.

Gold Deposit	Sample	Mineral for Age Determination and Method	Age (Ma)	Reference
Annage	Pyrite	Pyrite Re–Os	383 ± 8	[100]
Asiha	Ore	Monazite U–Pb	227.1 ± 6.5	[101]
Asiha	Granite porphyry	Zircon U–Pb	1	[101]
Caiyuanzi	Granodiorite porphyry	Zircon U–Pb	210.4 ± 1.9	[102]
Dashuigou	Tonalite	Zircon U–Pb	239.5 ± 0.9	[103]
Gerizhuotuo	Granodiorite	Zircon U–Pb	213.25 ± 0.62	[86]
Guoluolongwa	Pyrite and chalcopyrite	Sulfide Re–Os	374 ± 15	[100]
Baidungou	Quartz diorite	Zircon U–Pb	241.08 ± 0.90	[3]
Hongqigou	Dolerite	Zircon U–Pb	242.8 ± 2.1	[104]
Heishigou	Dolerite	Zircon U–Pb	244.1 ± 1.6	[3]
Kendekeke	Dacite tuffs	Zircon U–Pb	227.1 ± 1.2	[87]
Kendekeke	Monzogranite	Zircon U–Pb	229.5 ± 0.5	[88]
Kendekeke	Monzogranite	Zircon U–Pb	230.5 ± 4.2	[89]
Kengdenongshe	Ore-bearing rhyolitic tuffs	Zircon U–Pb	243.3 ± 1.6	[90]
Naomuhun	Sericite	Sericite Ar–Ar	227.84 ± 1.13	[91]
Naomuhun	Quartz diorite	Zircon U–Pb	235.8 ± 0.8	[91]
Xingshugou	Quartz albite porphyry	Zircon U–Pb	243.4 ± 1.9	[105]
Yanjingou	Ore	Quartz inclusion Rb–Sr	237 ± 3	[4]
Tuolugou	Pyrite	Pyrite Re–Os	429 ± 29	[106]

As for WGF, some previous studies reported the mineralization ages: [107,108] obtained the mica Ar-Ar age of 236 Ma and 242 Ma from the WGF, respectively; [4,109,110] obtained the zircon FT age, the fluid inclusion Rb-Sr age, the monazite U–Pb age and the zircon U–Pb age of 223, 237, 239, 244 Ma from the Yanjingou gold deposit; the 236.7 ± 3.7 Ma

age of Hongqigou deposit is similar with them. During that time, the Paleo-Tethys Ocean was under a transition period of flat subduction and slab rollback, which resulted in orogeny and magmatic activity, and released fluids from the subducted slab or the hydrated mantle wedge [111,112] which were conducive for generating the ore deposits in the region. However, the 422.2 ± 2.4 Ma age of the Huanglonggou deposit provide solid evidence that there was a metallogenic event during Paleozoic.

Based on the results of trace elements of pyrite, sulfur isotopic composition of sulfides and monazite U–Pb dating, we suggest that the WGF has undergone multiple-complex metallogenic processes based on multi-proxy studies, and that it can be interpreted as an orogenic gold field related to multiple tectonic–magmatic events.

7. Conclusions

(1) The monazite U–Pb ages of the Huanglonggou and Hongqigou deposits were 422.2 ± 2.4 Ma (MSWD = 0.16) and 236.7 ± 3.7 Ma (MSWD = 0.33), suggesting that there two epochs of metallogenic events that occured in the WGF.

(2) The ore-forming process can be divided into four hydrothermal stages: a quartz–pyrite stage (stage 1), a quartz–pyrite–arsenopyrite–chalcopyrite stage (stage 2), a quartz–galena–sphalerite–pyrite ± arsenopyrite ± chalcopyrite stage (stage 3) and a quartz–stibnite–carbonate stage (stage 4).

(3) Stages 1 and 2 are the main gold mineralization stages, wherein Au and As have a close genetic relationship. The Hongqigou and Huanglonggou deposits seem to be formed in different metallogenic events due to the contrast on the trace element compositions in pyrite.

(4) The source of ore-forming materials and fluids represented by δ34S and Co/Ni and Au/As ratios indicate that the Hongqigou and Huanglonggou deposits have apparent characteristics of orogenic gold deposit, and magmatic events happened during Paleozoic and Mesozoic made crucial contribution to their mineralization.

(5) We propose that the WGF went through multiple-complex metallogenic processes based on multi-proxy studies, and that this can be interpreted as an orogenic gold field related to multiple tectonic–magmatic events.

Author Contributions: Conceptualization, Z.Z. and Q.Z.; investigation, H.F., K.Y., X.L., G.L., J.W.; resources, H.X., Z.W., T.P.; writing—original draft preparation Z.Z.; writing—review and editing, Q.Z.; visualization, Q.Z.; supervision, Q.Z., H.F., K.Y.; funding acquisition, H.F., K.Y., Q.Z. All authors have read and agreed to the published version of the manuscript.

Funding: This work was funded by the Second Tibetan Plateau Scientific Expedition and Research Program (STEP) (No. 2019QZKK0801).

Institutional Review Board Statement: Not applicable.

Informed Consent Statement: Not applicable.

Data Availability Statement: Not applicable.

Acknowledgments: We are grateful to anonymous reviewers for constructive suggestions.

Conflicts of Interest: The authors declare no conflict of interest.

Appendix A

Table A1. The LA-ICP-MS analytical results of trace elements for different generations of pyrite in each stage and pyrrhotite in schist of wall rock in the Wulonggou Gold Field.

Sample	^{59}Co	^{60}Ni	^{65}Cu	^{66}Zn	^{75}As	^{107}Ag	^{121}Sb	^{125}Te	^{197}Au	^{208}Pb	^{209}Bi
Schist-Po-1	459.535	884.485	0.361	1.137	2.448	1.104	0.733	0.000	0.054	0.579	1.632
Schist-Po-2	491.131	1073.904	0.530	4.328	3.875	2.134	7.881	0.000	0.000	6.416	12.138
Schist-Po-3	436.918	746.358	0.228	1.853	0.000	1.977	0.284	0.461	0.084	1.560	2.543
Schist-Po-4	461.758	753.520	0.000	0.000	0.000	0.000	0.421	0.000	0.033	1.100	2.688
Schist-Po-5	433.093	832.637	1.453	7.117	2.040	2.240	5.391	0.000	0.000	8.720	13.182
Schist-Po-6	462.730	851.527	0.801	2.995	1.587	0.000	0.178	0.157	0.021	0.155	0.367
Schist-Po-7	326.323	591.205	1.949	5.291	4.594	0.000	15.199	0.000	0.124	3.610	2.674
Schist-Po-8	382.343	769.667	0.863	0.000	0.000	1.288	4.613	0.000	0.101	2.410	1.814
Ultramylonite-Py-1	989.711	158.880	29.096	3.412	1648.837	18.771	0.000	170.268	2.841	0.151	25.861
Ultramylonite-Py-2	73.199	66.455	43.764	3.898	6515.266	2.583	3.657	145.199	0.686	0.512	55.638
Ultramylonite-Py-3	239.699	1027.331	1290.252	8.683	456.654	10.258	2.022	161.739	0.000	0.020	23.681
Ultramylonite-Py-4	778.476	1663.032	54.432	7.999	1829.331	3.779	1.443	115.420	0.000	0.175	40.664
Ultramylonite-Py-5	2090.737	345.773	2124.885	2.923	534.603	2.355	3.283	192.794	0.248	0.096	46.837
Ultramylonite-Py-6	2045.162	798.940	753.049	5.934	455.063	3.733	2.382	196.658	0.000	0.029	49.249
Ultramylonite-Py-7	887.432	439.957	115.751	6.230	648.894	7.784	1.845	114.985	0.176	0.118	29.197
Ultramylonite-Py-8	298.831	30.788	25.344	0.937	6884.256	4.868	0.000	145.684	0.000	0.000	110.829
Hongqigou-Py1-1	32.496	55.501	256.376	1.585	34,711.167	1.453	196.130	0.000	1.545	46.914	0.102
Hongqigou-Py1-2	23.159	33.234	119.957	1.886	21,440.451	0.974	224.104	0.000	1.200	72.416	0.089
Hongqigou-Py1-3	44.046	56.473	200.034	0.000	31,916.973	0.000	313.303	2.123	1.684	86.845	0.253
Hongqigou-Py1-4	55.921	103.544	142.710	3.328	25,950.584	2.491	480.888	1.614	1.691	148.769	0.256
Hongqigou-Py1-5	23.500	27.524	360.547	2.609	56,807.293	0.000	113.957	0.000	1.115	23.523	0.136
Hongqigou-Py1-6	25.818	25.736	324.491	0.000	44,347.997	1.107	80.295	0.000	0.790	17.017	0.084
Hongqigou-Py2-1	84.478	162.908	504.067	0.000	57,046.708	0.000	64.167	0.000	0.668	16.123	0.305
Hongqigou-Py2-2	107.331	175.986	185.494	12.144	40,115.177	0.000	491.204	1.869	1.500	121.852	0.408
Hongqigou-Py2-3	159.267	242.640	366.549	2.229	50,364.569	3.160	243.525	0.000	0.263	74.326	0.621
Hongqigou-Py2-4	157.768	240.426	372.535	146.296	49,913.188	5.901	373.624	1.508	0.722	89.542	0.620
Hongqigou-Py2-5	73.299	102.625	483.004	0.000	76,993.084	0.000	138.039	0.000	0.616	29.056	0.306
Hongqigou-Py2-6	62.817	108.774	463.063	0.000	44,662.812	1.430	120.927	0.000	0.682	36.612	0.471
Hongqigou-Py2-7	81.504	204.076	607.798	0.000	57,651.922	1.140	51.747	0.000	0.606	10.809	0.068
Hongqigou-Py2-8	61.228	102.925	301.078	0.000	46,622.748	0.000	177.871	0.000	0.972	39.262	0.296
Hongqigou-Py2-9	57.332	121.853	589.064	0.000	67,080.552	1.399	135.813	0.000	3.447	25.224	0.203
Hongqigou-Py2-10	62.537	113.939	365.369	2.128	52,337.898	0.000	101.625	0.000	0.748	22.524	0.287
Hongqigou-Py3-1	0.372	5.640	4.065	3.334	3909.772	9.880	265.700	3.257	0.311	245.648	13.984
Hongqigou-Py3-2	32.846	21.510	0.737	0.000	3648.123	0.000	1.632	0.000	0.000	3.974	0.638
Hongqigou-Py3-3	46.389	19.667	1.367	0.000	4124.308	0.000	7.310	0.000	0.248	26.473	2.498
Hongqigou-Py3-4	0.036	0.000	1.285	0.000	2262.859	0.000	1.660	0.000	0.122	10.309	1.213
Hongqigou-Py3-5	0.115	0.000	0.747	0.000	2366.442	0.000	17.782	1.991	0.107	20.720	1.385
Hongqigou-Py3-6	0.088	0.000	2.524	1.517	5223.606	0.000	1.894	0.885	0.074	10.127	1.371
Hongqigou-Py3-7	0.286	0.000	0.985	0.000	3146.679	0.000	4.424	2.242	0.000	12.141	0.922
Hongqigou-Py3-8	10.640	17.532	15.724	3.974	2892.840	8.928	130.690	8.308	0.751	857.226	35.190
Hongqigou-Py3-9	6.045	3.601	3.910	0.000	2693.539	5.868	61.061	1.593	0.378	71.816	5.536
Huanglonggou-Py1-1	26.486	119.034	10.330	8.918	4662.131	0.000	0.000	99.793	1.071	0.454	60.713
Huanglonggou-Py1-2	53.938	16.091	37.423	5.330	2588.104	30.761	0.000	206.446	0.000	0.541	433.007
Huanglonggou-Py1-3	159.548	80.122	45.515	4.152	671.534	23.903	6.375	429.231	0.000	0.801	548.332
Huanglonggou-Py1-4	203.787	203.031	45.706	8.376	1233.971	17.891	7.261	390.036	0.445	0.755	761.660
Huanglonggou-Py1-5	52.195	89.540	27.779	6.579	732.027	14.941	2.718	220.313	0.000	0.568	420.303
Huanglonggou-Py1-6	14.371	58.264	16.535	0.000	6985.995	14.681	2.332	131.251	0.000	0.387	209.036
Huanglonggou-Py1-7	39.947	152.367	74.903	0.000	8270.601	0.000	29.734	916.985	0.000	1.414	264.691
Huanglonggou-Py1-8	152.760	313.391	86.059	2.255	5722.234	30.008	2.643	513.597	1.078	0.656	1210.961
Huanglonggou-Py1-9	84.559	122.308	64.932	4.021	8871.994	29.542	0.000	419.968	2.416	0.000	972.028
Huanglonggou-Py1-10	100.177	210.616	53.104	15.131	5297.483	47.119	1.799	333.662	0.000	0.342	800.335
Huanglonggou-Py2-1	7.537	61.689	6.086	0.000	5498.355	0.000	0.000	56.931	0.000	0.456	32.160
Huanglonggou-Py2-2	10.822	130.019	1.232	0.000	1575.172	0.000	0.000	10.803	0.000	0.143	4.263
Huanglonggou-Py2-3	135.063	56.744	25.632	2.440	250.834	15.419	2.932	178.409	0.000	0.135	269.836
Huanglonggou-Py2-4	1.646	39.854	12.457	0.000	2074.031	7.609	1.236	120.581	0.724	1.153	156.222
Huanglonggou-Py2-5	0.707	4.625	46.142	79.576	2193.181	4.008	11.649	460.266	1.229	0.000	76.231
Huanglonggou-Py2-6	43.340	147.200	54.534	7.673	13,275.196	19.131	7.322	348.155	0.000	0.592	167.483
Huanglonggou-Py2-7	1.268	8.446	5.126	1.594	4423.075	0.000	1.499	30.208	0.000	0.202	21.976
Huanglonggou-Py2-8	11.419	16.276	9.044	0.000	5415.672	5.730	0.000	17.236	0.527	0.271	32.765
Huanglonggou-Py3-1	8.533	4.247	9.788	5.692	3831.076	10.351	2.099	7.733	0.000	0.981	46.958
Huanglonggou-Py3-2	8.410	4.355	7.730	0.000	6464.305	11.060	3.567	20.651	0.000	2.423	503.080
Huanglonggou-Py3-3	7.393	10.818	6.513	2.156	3557.323	5.192	11.823	19.107	1.418	1.619	1853.086
Huanglonggou-Py3-4	12.274	2.107	2.553	0.000	11,409.009	9.809	0.000	3.573	0.000	4.018	15.335
Huanglonggou-Py3-5	27.731	56.888	14.968	0.000	8494.598	11.715	8.356	42.921	0.000	0.593	800.227
Huanglonggou-Py3-6	12.369	69.971	4.023	0.000	2636.416	8.345	0.000	8.120	0.000	0.238	46.526
Huanglonggou-Py3-7	7.310	18.067	2.135	0.000	612.995	11.731	0.000	9.519	0.000	0.128	17.815
Huanglonggou-Py3-8	11.240	5.630	5.456	2.840	9759.127	13.659	0.000	5.119	2.615	4.304	36.514
Huanglonggou-Py3-9	11.437	3.475	11.761	0.000	3335.870	0.000	5.096	28.996	1.354	1.118	754.925

References

1. Zhang, J.Y.; Ma, C.Q.; Li, J.W. Visible gold-forming environment evidenced by sulfide mineralogical characteristics of Shuizhadonggou-Huanglonggou gold deposit in eastern Kunlun orogen. *Miner. Depos.* **2012**, *31*, 1184–1194, (In Chinese with English abstract).
2. Zhang, J.Y.; Ma, C.Q.; Li, J.W.; Pan, Y.M. A possible genetic relationship between orogenic gold mineralization and post-collisional magmatism in the eastern Kunlun Orogen, western China. *Ore Geol. Rev.* **2017**, *81*, 342–357. [CrossRef]
3. Zhang, Y.T. *Research on Metallogenesis of Gold Deposits in the Wulonggou Ore Concentration Area, Central Segment of the East Kunlun Mountains, Qinghai Province*; Jilin University: Changchun, China, 2018; (In Chinese with English abstract).
4. Chen, B.L.; Wang, Y.; Han, Y.; Chen, J.L. Metallogenic age of Yanjingou gold deposit in Wulonggou gold orefield, eastern Kunlun Mountains. *Miner. Depos.* **2019**, *38*, 541–556, (In Chinese with English abstract).
5. Chen, J.J.; Wei, J.H.; Fu, L.B.; Li, H.; Zhou, H.Z.; Zhao, X.; Zhan, X.F.; Tan, J. Multiple sources of the Early Mesozoic Gouli batholith, Eastern Kunlun Orogenic Belt, northern Tibetan Plateau: Linking continental crustal growth with oceanic subduction. *Lithos* **2018**, *292–293*, 161–178. [CrossRef]
6. Qinghai Bureau of Geology and Mineral Resources (QBGMR). *Regional Geology of Qinghai Province*; Geological Publishing House: Beijing, China, 1991; pp. 1–662, (In Chinese with English abstract).
7. Jiang, C.F.; Yang, J.S.; Feng, B.G.; Zhu, Z.Z.; Zhao, M. *Opening-Closing Tectonics of the Kunlun Mountalns*; Geological Publishing House: Beijing, China, 1992; pp. 1–224, (In Chinese with English abstract).
8. Chen, N.S.; Wang, Q.Y.; Chen, Q.; Li, X.Y. Components and metamorphism of the basements of the Qaidam and Oulongbuluke micro-continental blocks, and a tentative interpretation of paleocontinental evolution in NW-Central China. *Earth Sci. Front.* **2007**, *14*, 43–55, (In Chinese with English abstract).
9. Ding, Q.F.; Yan, W.; Zhang, B.L. Sulfur-and lead-isotope geochemistry of the Balugou Cu-Pb-Zn skarn deposit in the Wulonggou area in the eastern Kunlun Orogen, NW China. *J. Earth Sci.* **2016**, *27*, 740–750. [CrossRef]
10. Chen, N.S.; Li, X.Y.; Zhang, K.X.; Wang, G.C.; Zhu, Y.H.; Hou, G.J.; Bai, Y.S. Lithological characteristics of the Baishahe formation to the south of Xiangride Town, Eastern Kunlun Mountains and its age constrained from zircon Pb–Pb dating. *Bull. Geol. Sci. Technol.* **2006**, *25*, 1–7, (In Chinese with English abstract).
11. Zhang, J.X.; Wan, Y.S.; Meng, F.C.; Yang, J.S.; Xu, Z.Q. Geochemistry, Sm-Nd and U-Pb isotope study of gneisses (schists) enclosing eclogites in the North Qaidam Mountains-deeply subducted Precambrian metamorphic basement? *Acta Petrol. Sin.* **2003**, *19*, 443–451, (In Chinese with English abstract).
12. Wang, G.C.; Wang, Q.H.; Jian, P.; Zhu, Y.H. Zircon SHRIMP ages of Precambrian metamorphic basement rocks and their tectonic significance in the eastern Kunlun Mountains, Qinghai Province, China. *Earth Sci. Front.* **2004**, *11*, 481–490, (In Chinese with English abstract).
13. Liu, Y.J.; Genser, J.; Neubauer, F.; Jin, W.; Ge, X.H.; Handler, R.; Takasu, A. 40Ar/39Ar mineral ages from basement rocks in the Eastern Kunlun Mountains, NW China, and their tectonic implications. *Tectonophysics* **2005**, *398*, 199–224. [CrossRef]
14. Meng, F.C.; Zhang, J.X.; Cu, M.H. Discovery of Early Paleozoic eclogite from the East Kunlun, Western China and its tectonic significance. *Gondwana Res.* **2013**, *23*, 825–836. [CrossRef]
15. Mo, X.X.; Luo, Z.H.; Deng, J.F.; Yu, X.H.; Liu, C.D.; Shen, H.W.; Yuan, W.M.; Liu, Y.H. Granitoids and crust growth in East-Kunlun Orogenic Belt. *Geol. J. China Univ.* **2007**, *13*, 403–414, (In Chinese with English abstract).
16. Zhang, B.W. *Study on Metalliferous Deposits Mineralization in Southern Qilian Orogenic Belt, Qinghai Province*; Jilin University: Changchun, China, 2010; (In Chinese with English abstract).
17. Yang, J.S.; Robinson, P.T.; Jiang, C.F.; Xu, Z.Q. Ophiolites of the Kunlun mountains, China and their tectonic implications. *Tectonophysics* **1996**, *258*, 215–231. [CrossRef]
18. Li, R.B.; Pei, X.Z.; Li, Z.C.; Liu, Z.Q.; Chen, G.C.; Chen, Y.X.; Wei, F.H.; Gao, J.M.; Liu, C.J.; Pei, L. Geological characteristics of Late Palaeozoic–Mesozoic unconformities and their response to some significant tectonic events in eastern part of Eastern Kunlun. *Earth Sci. Front.* **2012**, *19*, 244–254, (In Chinese with English abstract).
19. Li, X.W.; Huang, X.F.; Luo, M.F.; Dong, G.C.; Mo, X.X. Petrogenesis and geodynamic implications of the Mid-Triassic lavas from East Kunlun, northern Tibetan Plateau. *J. Asian Earth Sci.* **2015**, *105*, 32–47. [CrossRef]
20. Zhu, Y.H.; Pan, Y.M.; Zhang, K.X.; Chen, N.S.; Wang, G.C.; Hou, G.J. Mineralogical characteristics and petrogenesis of ophiolites in East Kunlun Orogenic Belt, Qinghai Province. *Acta Mineral. Sin.* **2000**, *20*, 128–142, (In Chinese with English abstract).
21. Bian, Q.T.; Li, D.H.; Pospelov, I.; Yin, L.M.; Li, H.S.; Zhao, D.S.; Chang, C.F.; Luo, X.Q.; Gao, S.L.; Astrakhantsev, O.; et al. Age, geochemistry and tectonic setting of Buqingshan ophiolites, North Qinghai-Tibet Plateau, China. *J. Asian Earth Sci.* **2004**, *23*, 577–596. [CrossRef]
22. Li, R.B.; Pei, X.Z.; Li, Z.C.; Sun, Y.; Feng, J.Y.; Lei, P.; Chen, G.C.; Liu, C.J.; Chen, Y.X. Geochemical features, age, and tectonic significance of the Kekekete mafic-ultramafic rocks, East Kunlun Orogen, China. *Acta Geol. Sin.* **2013**, *87*, 1319–1333.
23. Wei, B. *Study on the Geological Characteristic and Tectonic Attribute of the Ophiolite and Island-Arc-Type Igneous Rocks, Central Belt of East Kunlun (Eastern Section)*; Chang'an University: Xi'an, China, 2015; (In Chinese with English abstract).
24. Qi, X.P.; Yang, J.; Fan, X.G.; Cui, J.T.; Cai, Z.F.; Zeng, X.W.; Wei, W.; Qu, X.X.; Zai, L.M. Age, geochemical characteristics and tectonic significance of Changshishan ophiolite in central East Kunlun tectonic mélange belt along the east section of East Kunlun Mountains. *Geol. China* **2016**, *43*, 797–816, (In Chinese with English abstract).

25. Li, W.Y. *Geochronology and Geochemistry of the Ophiolites and Island-Arc-Type Igneous Rocks in the Western Qinling Orogen and the Eastern Kunlun Orogen: Implication for the Evolution of the Tethyan Ocean*; University of Science and Technology of China: Hefei, China, 2008; (In Chinese with English abstract).
26. Liu, Z.Q.; Pei, X.Z.; Li, R.B.; Li, Z.C.; Zhang, X.F.; Liu, Z.G.; Chen, G.C.; Chen, Y.X.; Ding, S.P.; Guo, J.F. LA-ICP-MS zircon U-Pb geochronology of the two suites of ophiolites at the Buqingshan area of the A'nyemaqen Orogenic Belt in the southern margin of East Kunlun and its tectonic implication. *Acta Geol. Sin.* **2011**, *85*, 185–194, (In Chinese with English abstract).
27. Chen, L.; Sun, Y.; Pei, X.Z.; Gao, M.; Feng, T. Northernmost paleo-tethyan oceanic basin in Tibet: Geochronological evidence from 40Ar/39Arage dating of Dur'ngoi ophiolite. *Chin. Sci. Bull.* **2001**, *46*, 1203–1205. [CrossRef]
28. Yin, A.; Harrison, T.M. Geologic evolution of the Himalayan-Tibetan orogen. *Annu. Rev. Earth Planet. Sci.* **2000**, *28*, 211–280. [CrossRef]
29. Roger, F.; Arnaud, N.; Gilder, S.; Tapponnier, P.; Jolivet, M.; Brunel, M.; Malavieille, J.; Xu, Z.Q.; Yang, J. Geochronological and geochemical constraints on Mesozoic suturing in east central Tibet. *Tectonics* **2003**, *22*, 1037. [CrossRef]
30. Zhang, J.Y.; Ma, C.Q.; Xiong, F.H.; Liu, B.; Li, J.W.; Pan, Y.M. Early Paleozoic high- Mg diorite-granodiorite in the eastern Kunlun Orogen, western China: Response to continental collision and slab break-off. *Lithos* **2014**, *210–211*, 129–146. [CrossRef]
31. Xiong, F.H.; Ma, C.Q.; Zhang, J.Y.; Liu, B.; Jiang, H.A. A reworking of old continental lithosphere: An important crustal evolutionmechanism in orogenic belts, as evidenced by Triassic I-type granitoids in the East Kunlun orogen, Northern Tibetan Plateau. *J. Geol. Soc.* **2014**, *171*, 847–863. [CrossRef]
32. Xiong, F.H.; Ma, C.Q.; Wu, L.; Jiang, H.A.; Liu, B. Geochemistry, zircon U-Pb ages and Sr-Nd-Hf isotopes of an Ordovician appinitic pluton in the East Kunlun orogen: New evidence for Proto-Tethyan subduction. *J. Asian Earth Sci.* **2015**, *111*, 681–697. [CrossRef]
33. Chen, X.H.; Gehrels, G.; Yin, A.; Zhou, Q.; Huang, P.H. Geochemical and Nd–Sr–Pb–O isotopic constrains on Permo–Triassic magmatism in eastern Qaidam Basin, northern Qinghai-Tibetan plateau: Implications for the evolution of the Paleo-Tethys. *J. Asian Earth Sci.* **2015**, *114*, 674–692. [CrossRef]
34. Wu, C.; Yin, A.; Zuza, A.V.; Zhang, J.Y.; Liu, W.C.; Ding, L. Pre-Cenozoic geologic history of the central and northern Tibetan plateau and the role of Wilson cycles in constructing the Tethyan orogenic system. *Lithosphere* **2016**, *8*, 254–292. [CrossRef]
35. Chen, N.S.; Zhang, L.; Sun, M.; Wang, Q.Y.; Kusky, T.M. U–Pb and Hf isotopic compositions of detrital zircons from the paragneisses of the Quanji Massif, NW China: Implications for its early tectonic evolutionary history. *J. Asian Earth Sci.* **2012**, *54–55*, 110–130. [CrossRef]
36. Dai, J.G.; Wang, C.S.; Jeremy, H.; Santosh, M. Multi-stage tectono-magmatic events of the Eastern Kunlun Range, northern Tibet: Insights from U-Pb geochronology and (U-Th)/He thermochronology. *Tectonophysics* **2013**, *599*, 97–106. [CrossRef]
37. Chen, Y.X.; Pei, X.Z.; Li, R.B.; Liu, Z.Q.; Li, Z.C.; Zhang, X.F.; Chen, G.C.; Liu, Z.G.; Ding, S.P.; Guo, J.F. Zircon U-Pb age of Xiaomiao Formation of Proterozoic in the Eastern section of the East Kunlun Orogenic Belt. *Geoscience* **2011**, *25*, 510–521, (In Chinese with English abstract).
38. Yu, C. *Characteristics of Metamorphic Rock Series and It's Fluid Inclusions from Jinshuikou in Eastern Kunlun*; Jilin University: Jilin, China, 2005; (In Chinese with English abstract).
39. Lu, L. *Study on the Ore-Controlling Structure of Wulonggou Gold Deposit in East Kunlun Mountain*; Chinese Academy of Geological Sciences: Beijing, China, 2011; (In Chinese with English abstract).
40. Liu, B.; Ma, C.Q.; Guo, P.; Zhang, J.Y.; Xiong, F.H.; Huang, J.; Jiang, H.A. Discovery of the middle Devonian A-type granite from the Eastern Kunlun Orogen and its tectonic implications. *Earth Sci. J. China Univ. Geosci.* **2013**, *38*, 947–962, (In Chinese with English abstract).
41. Zhang, D.Q.; Feng, C.Y.; Li, D.X.; Xu, W.Y.; Yan, S.H. Orogenic gold deposits in the North Qaidam and East Kunlun Orogen, West China. *Miner. Depos.* **2001**, *20*, 137–146, (In Chinese with English abstract).
42. Liu, Z.C.; Wu, F.Y.; Yang, Y.H.; Yang, J.H.; Wilde, S.A. Neodymium isotopic compositions of the standard monazites used in U-Th-Pb geochronology. *Chem. Geol.* **2012**, *334*, 221–239. [CrossRef]
43. Griffin, W.; Powell, W.; Pearson, N.; O'Reilly, S. GLITTER: Data reduction software for laser ablation ICP-MS. *Mineral. Assoc. Can.* **2008**, *40*, 308–311.
44. Danyushevsky, L.; Robinson, P.; Gilbert, S.; Norman, M.; Large, R.; McGoldrick, P.; Shelley, M. Routine quantitative multi-element analysis of sulphide minerals by laser ablation ICP-MS: Standard development and consideration of matrix effects. *Geochem. Explor. Environ. Anal.* **2011**, *11*, 51–60. [CrossRef]
45. Fu, J.; Hu, Z.; Zhang, W.; Yang, L.; Liu, Y.; Li, M.; Zong, K.; Gao, S.; Hu, S. In situ sulfur isotopes (delta (34)S and delta (33)S) analyses in sulfides and elemental sulfur using high sensitivity cones combined with the addition of nitrogen by laser ablation MC-ICP-MS. *Anal. Chim. Acta* **2016**, *911*, 14–26. [CrossRef]
46. Hu, Z.; Zhang, W.; Liu, Y.; Gao, S.; Li, M.; Zong, K.; Chen, H.; Hu, S. "Wave" signalsmoothing and mercury-removing device for laser ablation quadrupole and multiple collector ICPMS analysis: Application to lead isotope analysis. *Anal. Chem.* **2015**, *87*, 1152–1157. [CrossRef]
47. Zhang, W.; Hu, Z.; Liu, Y. Iso-Compass: New freeware software for isotopic data reduction of LA-MC-ICP-MS. *J. Anal. At. Spectrom.* **2020**, *35*, 1087–1096. [CrossRef]
48. Reich, M.; Kesler, S.E.; Utsunomiya, S.; Palenik, C.S.; Chryssoulis, S.L.; Ewing, R.C. Solubility of gold in arsenian pyrite. *Geochim. Cosmochim. Acta* **2005**, *69*, 2781–2796. [CrossRef]

49. Barker, S.L.L.; Hickey, K.A.; Cline, J.S.; Dipple, G.M.; Kilburn, M.R.; Vaughan, J.R.; Longo, A.A. Uncloaking invisible gold: Use of nano-SIMS to evaluate gold, trace elements, and sulphur isotopes in pyrite from Carlin-type gold deposits. *Econ. Geol.* **2009**, *104*, 897–904. [CrossRef]
50. Deditius, A.P.; Utsunomiya, S.; Ewing, R.C.; Chryssoulis, S.L.; Venter, D.; Kesler, S.E. Decoupled geochemical behavior of As and Cu in hydrothermal systems. *Geology* **2009**, *37*, 707–710. [CrossRef]
51. Deditius, A.P.; Utsunomiya, S.; Kesler, S.E.; Reich, M.; Ewing, R.C. Trace elements nanoparticles in pyrite. *Ore Geol. Rev.* **2011**, *42*, 32–46. [CrossRef]
52. Large, R.R.; Danyushevsky, L.; Hollit, C.; Maslennikov, V.; Meffre, S.; Gilbert, S.; Bull, S.; Scott, R.; Emsbo, P.; Thomas, H.V.; et al. Gold and trace element zonation in pyrite using a laser imaging technique: Implications for the timing of gold in orogenic and Carlin-Style sediment-hosted deposits. *Econ. Geol.* **2009**, *104*, 635–668. [CrossRef]
53. Deditius, A.P.; Reich, M.; Kesler, S.E.; Utsunomiya, S.; Chryssoulis, S.L.; Walshe, J.; Ewing, R.C. The coupled geochemistry of Au and As in pyrite from hydrothermal ore deposits. *Geochimica. Cosmochim. Acta* **2014**, *140*, 644–670. [CrossRef]
54. Gregory, D.; Meffre, S.; Large, R. Comparison of metal enrichment in pyrite framboids from a metal-enriched and metal-poor estuary. *Am. Mineral.* **2014**, *99*, 633–644. [CrossRef]
55. Tardani, D.; Reich, M.; Deditius, A.P.; Chryssoulis, S.; Sánchez-Alfaro, P.; Wrage, J.; Roberts, M.P. Copper-arsenic decoupling in an active geothermal system: A link betweenpyrite and fluid composition. *Geochim. Cosmochim. Acta* **2017**, *204*, 179–204. [CrossRef]
56. Heinrich, C.A.; Driesner, T.; Stefánsson, A.; Seward, T.M. Magmatic vapor contraction and the transport of gold from the porphyry environment to epithermal ore deposits. *Geology* **2004**, *32*, 761–764. [CrossRef]
57. Heinrich, C.A. Fluid-fluid interactions in magmatic-hydrothermal ore formation. *Rev. Mineral. Geochem.* **2007**, *65*, 363–387. [CrossRef]
58. Reich, M.; Deditius, A.; Chryssoulis, S.; Li, J.W.; Ma, C.Q.; Parada, M.A.; Barra, F.; Mittermayr, F. Pyrite as a record of hydrothermal fluid evolution in a porphyry copper system: A SIMS/EMPA trace element study. *Geochim. Cosmochim. Acta* **2013**, *104*, 42–62. [CrossRef]
59. Román, N.; Reich, M.; Leisen, M.; Morata, D.; Barra, F.; Deditius, A.P. Geochemical and micro-textural fingerprints of boiling in pyrite. *Geochim. Cosmochim. Acta* **2019**, *246*, 60–85. [CrossRef]
60. Cabri, L.J.; Chryssoulis, S.L.; de Villiers, J.P.; Laflamme, J.G.; Buseck, P.R. The nature of "invisible" gold in arsenopyrite. *Can. Miner.* **1989**, *27*, 353–362.
61. Cook, N.J.; Chryssoulis, S.L. Concentrations of invisible gold in the common sulfides. *Can. Miner.* **1990**, *28*, 1–16.
62. Morishita, Y.; Hammond, N.Q.; Momii, K.; Konagaya, R.; Sano, Y.; Takahata, N.; Ueno, H. Invisible gold in pyrite from epithermal, banded-iron-formation-hosted, and sedimentary gold deposits: Evidence of hydrothermal influence. *Minerals* **2019**, *9*, 447. [CrossRef]
63. Morishita, Y.; Shimada, N.; Shimada, K. Invisible gold in arsenian pyrite from the high-grade Hishikari gold deposit, Japan: Significance of variation and distribution of Au/As ratios in pyrite. *Ore Geol. Rev.* **2018**, *95*, 79–93. [CrossRef]
64. Kusebauch, C.; Gleeson, S.A.; Oelze, M. Coupled partitioning of Au and As into pyrite controls formation of giant Au deposits. *Sci. Adv.* **2019**, *5*, eaav5891. [CrossRef]
65. Fleet, M.E.; Wu, T.W. Volatile transport of platinumgroup elements in sulfide-chloride assemblages at 1000 °C. *Geochim. Cosmochim. Acta* **1993**, *57*, 3519–3531. [CrossRef]
66. Campbell, F.A.; Ethier, V.G. Nickel and colbalt in pyrrhotite and pyrite from the Faro and Sullivan ore bodies. *Can. Mineral.* **1984**, *22*, 503–506.
67. Bajwah, Z.U.; Seccombe, P.K.; Offler, R. Trace element distribution Co: Ni ratios and genesis of the Big Cadia iron-copper deposit, New South Wales, Australia. *Miner. Depos.* **1987**, *22*, 292–300. [CrossRef]
68. Koglin, N.; Frimmel, H.E.; Minter, W.E.L.; Brätz, H. Trace-element characteristics of different pyrite types in Mesoarchean to Paleoproterozoic placer deposits. *Miner. Depos.* **2010**, *45*, 259–280. [CrossRef]
69. Reich, M.; Simon, A.; Deditius, A.; Barra, F.; Chryssoulis, S.; Lagas, G.; Tardani, D.; Knipping, J.; Bilenker, L.; Sánchez-Alfaro, P.; et al. Trace element signature of pyrite from the Los Colorados Iron Oxide-Apatite (IOA) deposit, Chile: A missing link between Andean IOA and Iron Oxide Copper-Gold systems? *Econ. Geol.* **2016**, *111*, 743–761. [CrossRef]
70. Peterson, E.C.; Mavrogenes, J.A. Linking high-grade gold mineralization to earthquake-induced fault-valve processes in the Porgera gold deposit, Papua New Guinea. *Geology* **2014**, *42*, 383–386. [CrossRef]
71. Rye, R.O.; Ohmoto, H. Sulfur and carbon isotopes and ore genesis: A review. *Econ. Geol.* **1974**, *69*, 826–842. [CrossRef]
72. Ohmoto, H. Stable isotope geochemistry of ore deposit. *Rev. Mineral. Geochem.* **1986**, *16*, 491–559.
73. Ohmoto, H.; Goldhaber, M.B. *Sulfur and carbon isotopes, In Geochemistry of Hydrothermal ore Deposits*, 2nd ed.; Barnes, H.L., Ed.; John Wiley & Sons Inc.: New York, NY, USA, 1997; pp. 517–611.
74. Seal, R.R. Sulfur isotope geochemistry of sulfide minerals. *Rev. Mineral. Geochem.* **2006**, *61*, 633–677. [CrossRef]
75. Luhr, J.F.; Logan, M.A.V. Sulfur isotope systematics of the 1982 El Chich'on trachyandesite: An ion microprobe study. *Geochim. Cosmochim. Acta* **2002**, *66*, 3303–3316. [CrossRef]
76. Rollinson, H.R. *Using Geochemical Data: Evaluation, Presentation, Interpretation*; Routledge: London, UK, 1993; pp. 306–308.
77. Goldfarb, R.J.; Groves, D.I.; Gardoll, S. Orogenic gold and geologic time: A global synthesis. *Ore Geol. Rev.* **2001**, *18*, 1–75. [CrossRef]

78. Groves, D.I.; Santosh, M. Craton and thick lithosphere margins: The sites of giant mineral deposits and mineral provinces. *Gondwana Res.* **2021**, *100*, 195–222. [CrossRef]
79. Mernagh, T.P.; Bastrakov, E.N.; Zaw, K.; Wygralak, A.S.; Wyborn, L.A.I. Comparison of fluid inclusion data and mineralization processes for Australian orgenic gold and intrusion-related gold systems. *Acta Petrol. Sin.* **2007**, *23*, 21–32.
80. Goldfarb, R.J.; Baker, T.; Dube, B.; Groves, D.I.; Hart, C.J.R.; Gosselin, P. Distribution, character, and genesis of gold deposits in metamorphic terranes. In *100th Anniversary Volume*; Hedenquist, J.W., Thompson, J.F.H., Goldfarb, R.J., Richards, J.P., Eds.; Society of Economic Geologists: Littleton, CO, USA, 2005; pp. 407–450.
81. Dong, Y.P.; He, D.F.; Sun, S.S.; Liu, X.M.; Zhou, X.H.; Zhang, F.F.; Yang, Z.; Cheng, B.; Zhao, G.C.; Li, J.H. Subduction and accretionary tectonics of the East Kunlun orogen, western segment of the Central China Orogenic System. *Earth Sci. Rev.* **2018**, *186*, 231–261. [CrossRef]
82. Zhang, L.; Chen, R.X.; Zheng, Y.F.; Li, W.C.; Hu, Z.C.; Yang, Y.H.; Tang, H.L. The tectonic transition from oceanic subduction to continental subduction: Zirconological constraints from two types of eclogites in the North Qaidam orogen, northern Tibet. *Lithos* **2016**, *244*, 122–139. [CrossRef]
83. Wang, M.J.; Song, S.G.; Niu, Y.L.; Su, L. Post-collisional magmatism: Consequences of UHPM terrane exhumation and orogen collapse, N. Qaidam UHPM belt, NW China. *Lithos* **2014**, *210*, 181–198. [CrossRef]
84. Wu, C.; Zuza, A.V.; Chen, X.; Ding, L.; Levy, D.A.; Liu, C.; Liu, W.; Jiang, T.; Stockli, D.F. Tectonics of the Eastern Kunlun Range: Cenozoic Reactivation of a Paleozoic—Early Mesozoic Orogen. *Tectonics* **2019**, *38*, 1609–1650. [CrossRef]
85. Tomkins, A.G. On the source of orogenic gold. *Geology* **2013**, *41*, 1255–1256. [CrossRef]
86. Li, J.Q.; Wang, T.; Chen, J.; Bai, Z.H.; Lin, Y.H. Zircon U-Pb age and petrogeochemical characteristics of ore-hosting granodiorite in Manite gold deposit, East Kunlun. *J. Mineral. Petrol.* **2019**, *39*, 69–77, (In Chinese with English abstract).
87. Pan, X.P.; Li, R.S.; Yu, P.S.; Gu, P.Y.; Shi, C.; Wang, C.; Cha, X.F. The age of country rocks of the Kendekeke Fe-Co polymetalic deposit in Qimantag area and its significance. *Acta Petrol. Mineral.* **2013**, *32*, 53–62, (In Chinese with English abstract).
88. Xiao, Y.; Feng, C.Y.; Liu, J.N.; Yu, M.; Zhou, J.H.; Li, D.X.; Zhao, Y.M. LA-MC-ICP-MS zircon U-Pb dating and sulfur isotope characteristics of Kendekeke Fe-polymetallic deposit, Qinghai Province. *Miner. Depos.* **2013**, *32*, 177–186, (In Chinese with English abstract).
89. Xi, R.G.; Xiao, P.X.; Wu, Y.Z.; Dong, Z.C.; Guo, L.; Gao, X.F. The geological significances, composition and age of the monzonitic granite in Kendekeke iron mine. *Northwest. Geol.* **2010**, *43*, 195–202, (In Chinese with English abstract).
90. Liang, Y.Y.; Xia, R.; Shan, X.Y.; Ma, Y.; Zhao, E.Q.; Guo, W.H. Geochronology and Geochemistry of Ore-Hosting Rhyolitic Tuff in the Kengdenongshe Polymetallic Deposit in the Eastern Segment of the East Kunlun Orogen. *Minerals* **2019**, *9*, 589. [CrossRef]
91. Li, J.C.; Kong, H.L.; Li, Y.Z.; Namkha, N.; Jia, Q.Z.; Guo, X.Z.; Zhang, B. Ar-Ar age of altered sericite, zircon U-Pb age of quartz diorite and geochemistry of the Naomuhun gold deposit, east Kunlun. *Acta Geol. Sin.* **2017**, *91*, 979–991, (In Chinese with English abstract).
92. Song, S.G.; Niu, Y.L.; Su, L.; Xia, X.H. Tectonics of the North Qilian orogen, NW China. *Gondwana Res.* **2013**, *23*, 1378–1401. [CrossRef]
93. Xiao, Y.; Feng, C.Y.; Li, D.X.; Liu, J.N. Chronology and fluid inclusions of the Guoluolongwa gold deposit in Qinghai Province. *Acta Geol. Sin.* **2014**, *88*, 895–902, (In Chinese with English abstract).
94. Xia, R.; Wang, C.; Deng, J.; Carranza, E.J.M.; Li, W.; Qing, M. Crustal thickening prior to 220Ma in the East Kunlun Orogenic Belt: Insights from the Late Triassic granitoids in the Xiao-Nuomuhong pluton. *J. Asian Earth Sci.* **2014**, *93*, 193–210. [CrossRef]
95. Wang, W.; Yuan, W.M.; Gou, J.; Tian, C.S.; Ma, Z.Y.; Peng, W.X.; Feng, Y.L.; Cao, J.H.; Cheng, X.Q.; Hao, N.N. Zircon U-Pb ages and geochemical features of granites in Dulan area, Eastern Kunlun Mountains. *J. Chin. Electron Microsc. Soc.* **2015**, *34*, 222–233, (In Chinese with English abstract).
96. Chen, J.J.; Fu, L.B.; Wei, J.H. Geochemical characteristics of Late Ordovician granodiorite in Gouli area, Eastern Kunlun orogenic belt, Qinghai province: Implications on the evolution of Proto-Tethys Ocean. *Earth Sci.* **2015**, *41*, 1863–1882, (In Chinese with English abstract).
97. Guo, X.Z.; Jia, Q.Z.; Kong, H.L.; Li, Y.Z.; Li, J.C.; Ma, Z.Y.; Wang, Y. Zircon U-Pb geochronology and geochemistry of Harizha quartz diorite in the eastern section from East Kunlun. *Geol. Sci. Technol. Inf.* **2016**, *35*, 18–26, (In Chinese with English abstract).
98. Fan, X.Z.; Sun, F.Y.; Xu, C.H.; Xin, W.; Wang, Y.C.; Zhang, Y. Genesis of Harizha Ag-Pb-Zn deposit in the eastern Kunlun Orogen, NW China: Evidence of fluid inclusions and C-H-O-S-Pb isotopes. *Resour. Geol.* **2021**, *71*, 177–201. [CrossRef]
99. Li, J.C.; Jia, Q.Z.; Du, W.; Li, Y.Z.; Kong, H.L.; Namkha, N.; Yang, B.R. LA-ICP-MS zircon dating and geochemical characteristics of quartz diorite in Asiha gold deposit in East segment of Eastern Kunlun. *J. Jilin Univ. (Earth Sci. Edi.)* **2014**, *44*, 1188–1199, (In Chinese with English abstract).
100. Chen, J.J.; Fu, L.B.; David, S.; Wei, J.H.; Zhao, X.; Zhou, H.Z. Multiple episodes of gold mineralization in the East Kunlun Orogen, western Central Orogenic Belt, China: Constraints from Re-Os sulfide geochronology. *Ore Geol. Rev.* **2020**, *123*, 103587. [CrossRef]
101. Liang, G.Z.; Yang, K.F.; Sun, W.Q.; Fan, H.R.; Li, X.H.; Lan, T.G.; Hu, H.L.; Chen, Y.W. Multistage ore-forming processes and metal source recorded in texture and composition of pyrite from the Late Triassic Asiha gold deposit, Eastern Kunlun Orogenic Belt, western China. *J. Asian Earth Sci.* **2021**, *220*, 104920. [CrossRef]
102. Yang, X.M. *Study on the Geological Characteristics and the Genesis of Caiyuanzi Gold Deposit in Easter Kunlun Orogenic Belt, Qinghai Province*; Jilin University: Changchun, China, 2019; (In Chinese with English abstract).

103. Li, J.C.; Du, W.; Cheng, Y.S.; Kong, H.L.; Liu, J.X.; Li, Y.Z.; Jia, Q.Z.; Namkha, N.; Xia, M.Z.; Li, Y.J. Characteristics of gold deposits and ore-control factors in the East Kunlun mineralization belt, Qinghai Province. *Geol. Explor.* **2015**, *51*, 1079–1088, (In Chinese with English abstract).
104. Cheng, L. *Study on the Geological and Geochemical Characteristics and Genesis of Hongqigou Gold Deposit, Wulonggou Ore Concentration Area, East Kunlun, Qinghai Province*; Jilin University: Changchun, China, 2020; (In Chinese with English abstract).
105. Shi, C.; Li, R.S.; He, S.P.; Yu, P.S.; Wang, C.; Pan, S.J.; Zhang, H.D. A preliminary study of the Xingshugou gold mineralization spots in the eastern segment of Kunlun orogenic belt and the dating of its surrounding rocks. *Geol. Bull. China* **2012**, *31*, 1983–1990, (In Chinese with English abstract).
106. Feng, C.Y.; Qu, W.J.; Zhang, D.Q.; Dang, X.Y.; Du, A.D.; Li, D.X.; She, H.Q. Re–Os dating of pyrite from the Tuolugou stratabound Co (Au) deposit, eastern Kunlun Orogenic Belt, northwestern China. *Ore Geol. Rev.* **2009**, *36*, 213–230. [CrossRef]
107. Zhang, D.Q.; Dang, X.Y.; She, H.Q.; Li, D.X.; Feng, C.Y.; Li, J.W. Ar-Ar dating of orogenic gold deposits in northern margin of Qaidam and East Kunlun Mountains and its geological significance. *Miner. Depos.* **2005**, *24*, 87–98, (In Chinese with English abstract).
108. Kou, L.L.; Luo, M.F.; Zhong, K.H.; Zhao, C.X. 40Ar/39Ar dating of the I goldbearing shear zone on the gold ore collected belt of the Wulonggou, Qinghai, and its significance. *Xinjiang Geol.* **2010**, *28*, 330–333, (In Chinese with English Abstract).
109. Yuan, W.M.; Mo, X.X.; Zhang, A.K.; Chen, X.N.; Duan, H.W.; Li, X.; Hao, N.N.; Wang, X.M. Fission track thermochronology evidence for multiple periods of mineralization in the Wulonggou gold deposits, Eastern Kunlun Mountains, Qinghai Province. *J. Earth Sci.* **2013**, *24*, 471–478. [CrossRef]
110. Wu, J.J.; Zeng, Q.D.; Santosh, M.; Fan, H.R.; Wei, Z.H.; Yang, K.F.; Zhang, Z.M.; Li, X.H.; Liang, G.Z. Intrusion-related orogenic gold deposit in the East Kunlun belt, NW China: A multiproxy investigation. *Ore Geol. Rev.* **2021**, *139*, 104550. [CrossRef]
111. Goldfarb, R.J.; Groves, D.I. Orogenic gold: Common or evolving fluid and metal sources through time. *Lithos* **2015**, *233*, 2–26. [CrossRef]
112. Groves, D.I.; Santosh, M. The giant Jiaodong gold province: The key to a unified model for orogenic gold deposits? *Geosci. Front.* **2016**, *7*, 409–417. [CrossRef]